Analysis of a Heavy Rainfall Event during TAMEX

JUN LI AND YI-LENG CHEN

Department of Meteorology, School of Ocean and Earth Science and Technology, University of Hawaii at Manoa, Honolulu, Hawaii

WEN-CHAU LEE

National Center for Atmospheric Research, Boulder, Colorado

(Manuscript received 25 October 1995, in final form 12 September 1996)

ABSTRACT

A heavy rainfall event during the Taiwan Area Mesoscale Experiment intensive observing period 13 has been studied using upper-air, surface mesonet, and dual-Doppler radar data. The heavy rainfall ($\geq$231 mm day^{-1}) occurred over northwestern Taiwan with the maximum rainfall along the northwestern coast and was caused by a long-lived, convective rainband in the prefrontal atmosphere. It occurred in an upper-level divergence region and along the axis of the maximum equivalent potential temperature at the 850-hPa level.

As a Mei-Yu front advanced southeastward, the postfrontal cold air in the lowest levels was retarded by the hilly terrain along the southeastern China coast. As a result, a low-level wind-shift line associated with a pressure trough at the 850-hPa level moved over the Taiwan Strait before the arrival of the surface front. The westerly flow behind the trough interacted with a barrier jet along the northwestern coast of Taiwan. The barrier jet is caused by the interaction between the prefrontal southwest monsoon flow and the island obstacle. A low-level convergence zone ($\sim$3 km deep) was observed along the wind-shift line between the westerly flow coming off the southeastern China coast and the barrier jet. A long-lived rainband developed within the low-level convergence zone and moved southeastward toward the northwestern Taiwan coast with the wind-shift line.

There were several long-lived ($>$2 h) reflectivity maxima embedded in the rainband. They often had several individual cells with a much shorter lifetime. The reflectivity maxima formed on the southwestern tip of the rainband and along the low-level wind-shift line. They intensified during their movement from the southwest to the northeast along the rainband. The continuous generation of the reflectivity maxima along the wind-shift line and the intensification of them over the low-level convergence zone maintained the long lifetime of the rainband and produced persistent heavy rainfall along the northwestern coast as these reflectivity maxima moved toward the coast. During the early stage of their lifetime, the reflectivity maxima were observed along the wind-shift line with upward motion in the lower troposphere. As they moved toward the northeastern part of the rainband and matured, the reflectivity maxima were observed southeast of the convergence zone with sinking motion in the lower troposphere. The upward motion was rooted along the wind-shift line and tilted southeastward with height. The reflectivity maxima dissipated as they moved inland. During the early stage of the rainband, the reflectivity maxima on the northeastern part of the rainband also merged with the convective line associated with the land-breeze front offshore of the northwestern coast.

The Mei-Yu front was shallow ($<$1 km) and moved slowly southward along the western coast. Convection associated with the front was weak with echo tops ($\sim$10 dBZ) below 6 km.

1. Introduction

With a steep topography and a narrow basin over the island of Taiwan, heavy rainfall during the early summer rainy season (May–June) frequently produces flash flooding. Over the last decade, the damage caused by a typical heavy rainfall–flash flood event over Taiwan is about 100–300 million U.S. dollars (Kuo and Chen 1990). The Taiwan Area Mesocale Experiment (TAMEX), jointly conducted by Taiwan and the United States during May–June 1987, is the first field experiment to focus on heavy rain problems over a mountainous island in the subtropics.

During 24–25 June 1987, heavy rain fell over northwestern Taiwan with the maximum rainfall along the northwestern coast ($\sim$231 mm day^{-1}; Trier 1990). This heavy rain event was not forecast correctly. Based on the Japanese Meteorological Agency model prediction, the forecast on the morning of 24 June called for a pressure ridge to build up over the Taiwan area for the next few days with only a slight chance for deep convection over the Taiwan Strait (Cunning 1988). An upper-level trough was located north of Taiwan, and it was expected to move east of Taiwan. Thus, a normal down day was declared after the 1000 LST briefing on 24

Corresponding author address: Dr. Yi-Leng Chen, Department of Meteorology, SOEST, University of Hawaii at Manoa, Honolulu, HI 96822.
E-mail: dave@soest.hawaii.edu

June. TAMEX intensive observing period (IOP) 13 was not initiated until 2200 LST 24 June after intense convection was observed over the Taiwan Strait. In this study, both the synoptic-scale conditions favorable for the development of heavy rainfall and the mesoscale circulations in determining the rainfall distributions will be analyzed using conventional and radar data.

The strong low-level southwesterly flow in the lower troposphere [so-called low-level jet or LLJ if the wind speed is at least 12.5 m s^{-1} at 850 hPa and 15 m s^{-1} at 700 hPa, Chen and Yu (1988)], which develops on the warm side of a cold front, is one of the important synoptic-scale features frequently accompanying heavy rainfall during the early summer rainy season over the Taiwan area. The LLJ transports warm, moist air from the south in low levels to generate convective instability and to lower the level of free convection (Chen 1983) all of which are favorable for the development of heavy precipitation. During TAMEX, the prefrontal southwesterly monsoon flow often reached the LLJ intensity. However, some of these LLJs failed to produce heavy rainfall over the Taiwan area (Cunning 1988). For the 24–25 June 1987 case, a strong southwesterly flow prevailed in the low-level prefrontal atmosphere over southeastern China and the Taiwan area as a Mei-Yu front approached. In contrast to the heavy rain over northwestern Taiwan, only scattered showers occurred over southeastern China associated with the Mei-Yu front, although copious moisture within the low-level warm, moist southwesterly monsoon flow also existed there.

The heavy rainfall-producing storms often occur within a few hundred kilometers of the Mei-Yu front (Chen and Chi 1980). Prior to TAMEX, it was suggested that the Mei-Yu frontal circulation was driven by a CISK (conditional instability of the second kind) process (Chen and Chang 1980; Chou et al. 1990). Chen (1993) found that during TAMEX, a seasonal transition occurred in mid-June 1987 during which the large-scale circulations experienced significant changes. After the seasonal transition, the semi-permanent south Asian anticyclone moves into southern China and the Tibetan Plateau, preventing upper-level baroclinic systems from moving into southern China and the Taiwan area. In contrast to the early studies, analysis of an early season heavy rain event (during 21–23 May 1987) along the southeastern China coast shows that the coupling between the upper-level baroclinic forcing and the low-level conditions is important for the development of heavy rainfall for this early season case (Chen and Li 1995a). The large-scale circulations favorable for the development of heavy rainfall after the seasonal transition may be different from those of the early season cases. In this study, we will first study the large-scale conditions favorable for the development of heavy precipitation for this late season case and compare them with those of the early season event (i.e., 21–23 May 1987).

Although widespread precipitation is generally regulated by large-scale conditions, the impacts of the orography can be crucial in focusing heavy rainfall on certain regions. For the early summer rainy season over Taiwan, large total rainfall amount and high heavy-rainfall frequency are frequently observed on the western side of the central mountain range with distinct local maxima along the foothills (Chen and Yang 1988). Observational studies have shown that the low-level wind field in the vicinity of Taiwan is also affected by the terrain and land–sea thermal contrasts (Chen and Hui 1990, 1992; Trier et al. 1990). Using aircraft, sounding, and surface mesonet data collected during TAMEX, Chen and Li (1995b) found a strong low-level barrier jet along the northwestern coast caused by the interaction between the prevailing southwest monsoon flow and the island topography. Furthermore, the nighttime offshore (downslope) flow from the island may intercept the prevailing southwesterly monsoon flow to form an enhanced region of low-level convergence, which may trigger convection (Kuo and Chen 1990).

In addition to the orographic effects over Taiwan, the hilly terrain along the southeastern China coast may also affect the movement of the frontal systems. Based on a TAMEX case (13–14 May) study, Chen and Hui (1992) found that the cold air behind the surface front was blocked by the hilly terrain and ducted around the southeastern China coast. As a result, the pressure trough at the 850-hPa level moved off the southeastern China coast before the postfrontal cold northeasterly flow arrived at the surface (their Fig. 11). The 850-hPa trough moved over the Taiwan Strait and western Taiwan before the surface front arrived.

To date, the 24–25 June heavy rainfall case has been studied by several investigators. Lin et al. (1989) showed that long-lived ($\sim$2 h) rain cells associated with the rainband were located along a wind shear line where the westerlies converged with the southwesterlies. Jou and Deng (1992) proposed that the heavy precipitation was caused by the convergence on the cyclonic side of the LLJ and the interaction between the LLJ and convective downdrafts in the frontal zone. Lin et al. (1992) stressed that the frontal lifting was responsible for the initiation of convection. They analyzed the rainband structure using dual-Doppler analysis of two volume scans at 0653 and 0700 LST and suggested that the maintenance of the rainband was caused by 1) frontal lifting, 2) a gust front arising from the convective downdrafts ahead of the front, and 3) discrete development of heavy rain cells in advance of the rainband. Although these studies, based on analyses of a few volume scans, were in general agreement that the rainband was located in the mesoscale low-level convergence zone, the nature of this low-level convergence is not well understood. The description of the evolution of the rainband is also lacking. Furthermore, these studies did not explain why the maximum rainfall was localized along the northwestern coast and did not fully consider the influence

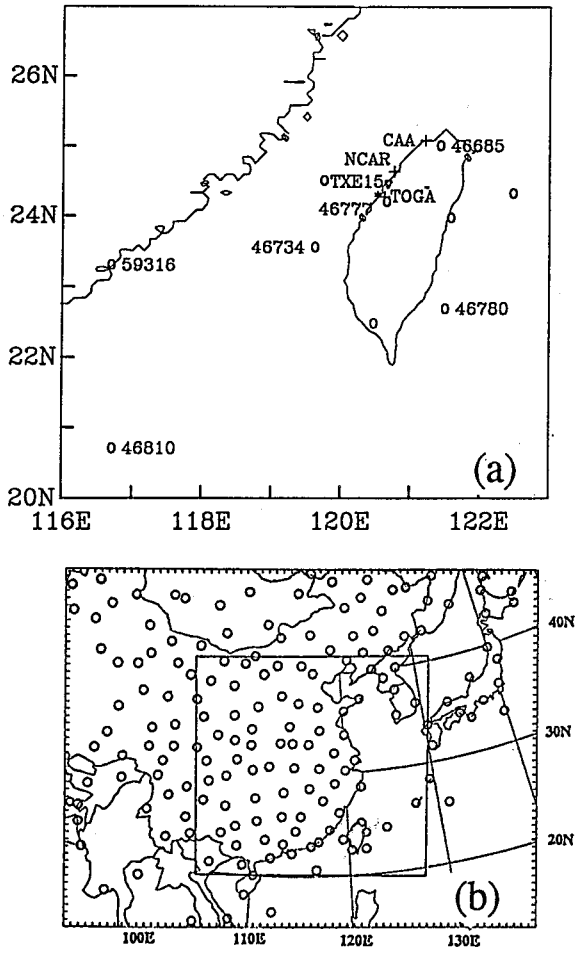

FIG. 1. (a) Doppler radar (+) positions, and the selected sounding (○), surface (*), and tower (▽) stations in this study. (b) Location of sounding stations used for the synoptic-scale analysis. The boxed area indicates the region over which the diagnostic results are shown.

of local circulations and orographic effects on the development of heavy rainfall. In this study, we will show that under favorable large-scale conditions for the development of heavy precipitation, the barrier jet along the northwestern coast of Taiwan and the orographic effects caused by the hilly terrain along the southeastern China coast are important to focus the heavy rainfall along the northwestern Taiwan coast.

2. Data type and analysis procedures

a. Dual-Doppler network and analysis

During TAMEX, the Doppler radar network consisted of three ground-based C-band Doppler radars positioned along the northwestern coast of Taiwan (Fig. 1a). The radars are owned by the Civil Aeronautics Administration (CAA) of the Republic of China, the National Center for Atmospheric Research (NCAR), and the National Oceanic and Atmospheric Administration (NOAA), Office of Tropical Ocean Global Atmosphere (TOGA), respectively. During IOP 13, the CAA, NCAR CP4, and TOGA radars started to collect data around 2200 LST 24 June, and 0110 LST and 0650 LST 25 June, respectively. To examine the detailed vertical structure of the low-level flow along the coast and its evolution during the heavy rain event, the velocity–azimuth display (VAD; Browning and Wexler 1968) is used to obtain the average wind profiles from each radar measurement.

To study the structure of the barrier jet along the coast, the mesoscale airflow, and the evolution of the rainband, we perform dual-Doppler analyses for the period from 0220 to 0422 LST 25 June during which the heavy rainfall started along the northwestern coast. Noise, ground-clutter contaminated data, and the second trip echoes are discarded, and aliased Doppler velocities are unfolded using the NCAR Research Data Support System (RDSS) (Oye and Carbone 1981). The edited data are then interpolated from spherical coordinates onto Cartesian grids. As usual, the steady-state assumption is made during the sampling period of approximately 5 min. The wind synthesis and subsequent computations in the dual-Doppler analysis are performed using NCAR's CEDRIC (custom editing and display of reduced information in Cartesian space) software package (Mohr et al. 1986). The terminal velocities of scatters are estimated with the empirical reflectivity-weighted formula (Atlas et al. 1973). Vertical velocities are obtained by downward integration of the anelastic mass-continuity equation from the upper to lower boundaries where vertical velocities are constrained to vanish.

The derived wind fields from Doppler radar data contain both random and nonrandom errors that can be introduced in the collection and analysis of the radial velocities from several sources. With limited collection times, temporal errors are caused by the advection and evolution of storm. The errors induced by storm evolution during the data collection time are nonrecoverable. In this study, the advection errors are corrected by introducing storm motion into the dual-Doppler analysis. Another source of error is the poorly sampled divergence near the earth's surface. This may be the largest source of error in estimating the vertical velocities. According to Doviak et al. (1976), Wilson et al. (1984), and Lee et al. (1992), the statistical uncertainties are usually less than 2 m s^{-1} for the derived horizontal winds and 4 m s^{-1} for the vertical velocities.

b. Surface network

During TAMEX, the surface network consisted of 74 surface observation stations, 126 rain gauges, and 21 wind tower stations. Wind speed and direction, temperature, and rainfall were recorded at most surface stations every hour, increasing to every half-hour during IOPs. Surface pressure and dewpoint temperature were observed at limited sites (Cunning 1988). The tower stations measured the wind speed and direction every 10 min at a height of ~10 m above the ground. Quality

checking for the surface data was made at the U.S. TAMEX Data Center of NCAR (Chen and Schumann 1990). The resolutions for wind speed, wind direction, pressure, temperature, dewpoint, and rainfall are 0.1 m s^{-1}, 1°, 0.1 hPa, 0.1°C, 0.1°C, and 0.1 mm h^{-1}, respectively. In this study, all the surface maps are analyzed subjectively.

c. Large-scale objective analysis

To study the large-scale conditions favorable for the development of heavy precipitation, routine upper-air sounding data are objectively analyzed every 12 h over a domain covering most of east Asia (Fig. 1b). All soundings within the region are reviewed manually and erroneous data are removed. Height, temperature, relative humidity, and winds are vertically interpolated to constant pressure surfaces (19 levels) from the 1000-hPa level to the 100-hPa level in 50-hPa increments at each station. The rawinsonde data are analyzed using Cressman's (1959) objective analysis scheme with an 80-km grid spacing. The mean station separation is about 260 km. The ratio between the grid spacing and the mean station separation is about 0.33, which is in the typical range of about 0.3–0.5 suggested by Koch et al. (1983). Synoptic-scale surface observations and ship reports are also analyzed and combined with the upper-air objective analysis. The analysis procedures used are identical to those of Chen et al. (1994).

3. Overview of weather conditions

In this section, we will first present the distribution of 2-h accumulated rainfall over the Taiwan area. Then, we will identify the synoptic-scale conditions favorable for the development of heavy rainfall. The orographic influence on the frontal movement and the prefrontal airflow will also be discussed.

a. Rainfall distributions

During the heavy rainfall episode, the rain fell mainly along the northwestern coast ahead of the surface front (Fig. 2). During 0300–0500 LST, the maximum 2-h accumulated rainfall (~50 mm) was located about 35 km south of the surface front over northwestern Taiwan (Fig. 2a). The rainfall increased significantly from 0500 to 0900 LST 25 June (Figs. 2b,c). The heaviest rainfall occurred during 0700–0900 LST with a maximum rain rate of 107 mm per 2 h along the northwestern coast (Fig. 2c). During the heavy rainfall period along the northwestern coast, light to moderate rain (≤20 mm per 2 h) was observed around the surface front. In the following hours, the major rainfall area shifted to the central western coast and the rain rate decreased significantly (Figs. 2d–f). During 1300–1500 LST, only light to moderate rain (~33 mm per 2 h) was observed over the western coast with light rain over the southwestern mountain slopes. Little precipitation was associated with the surface front at this time (Fig. 2f).

During the heavy rainfall along the northwestern coast, light precipitation was observed over the southwestern slopes of the central mountain range and mountain areas (Fig. 2). Light rainfall also occurred on the northeastern slopes in the postfrontal region (Figs. 2a–c). The rainfall over the southwestern slopes was mainly caused by the orographic lifting of the prefrontal southwesterly flow, whereas the rainfall on the northeastern slopes was related to the orographic lifting of the postfrontal northeasterly flow. Little precipitation was found at stations along the eastern coast (Fig. 2). This was partly because of the orographic blocking of the low-level warm, moist southwesterly monsoon flow. On the lee side, low-level drying and warming occurred at station 46780 (22.68°N, 121.50°E; Fig. 1b) because of the subsidence associated with midlevel westerly flow crossing the central mountain range with a shallow inversion below the 900-hPa level (not shown). Figure 2 is consistent with the detailed surface analysis of rainfall, surface frontal position, and winds over Taiwan with a 30-min interval presented by Chen (1991).

b. Synoptic overview

On 24 June 1987, a low pressure system moved eastward and deepened off the eastern China coast (Fig. 3). At 1200 UTC 24 June, a few hours prior to the development of the heavy precipitation over northwestern Taiwan, the low pressure center at the 850-hPa level was located at 29°N, 129°E (Fig. 3a). Over southern China and the Taiwan area, the low-level southwesterly monsoon flow brought in the warm, moist air from Indochina. Large equivalent potential temperature gradients were observed between the warm, moist monsoon airflow and the relatively dry and cold northeasterly flow behind the low pressure system. A pressure trough extended from the low pressure center to the southeastern China coast. The southern portion of the pressure trough was located over northern Taiwan Strait and within the region of high equivalent potential temperature (Fig. 3a). The southern part of the trough was characterized by a wind shift from southwesterly flow ahead of the trough to westerly behind. At 0000 UTC 25 June, the southern portion of the wind-shift line was near the northwestern coast of Taiwan (not shown).

The sounding for station 46685 (25.0°N, 121.4°E; Fig. 1a) over northern Taiwan (Fig. 4) showed that at 1200 UTC 24 June the atmosphere was conditionally unstable over the prefrontal, warm, and moist southwesterly monsoon flow. The convective available potential energy was 1136 $m^2 s^{-2}$, estimated by integrating the ''positive area'' on the skew T–log$p$ diagram between the temperature profile and the moist-adiabatic curve for an air parcel in the lowest 50 hPa. The positive area was generally ''skinny'' through a deep layer between 2.2 and 13 km, which was a typical feature for

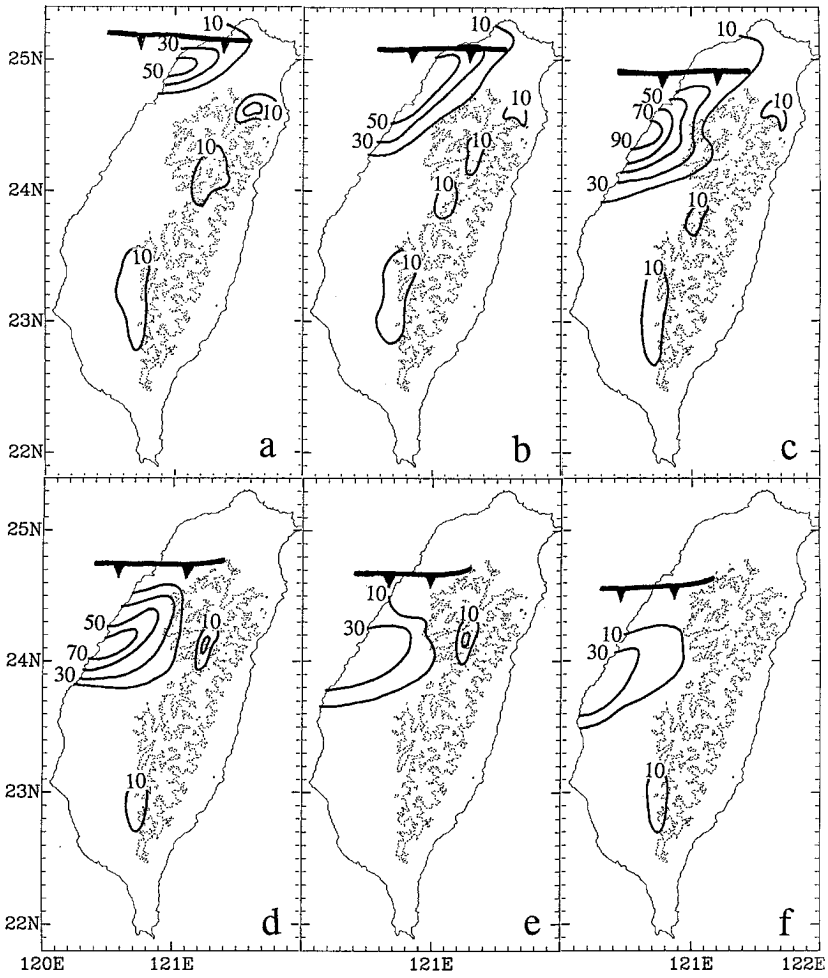

FIG. 2. Distributions of 2-h accumulated rainfall over the Taiwan area on 25 June 1987. (a) 0300–0500 LST, (b) 0500–0700 LST, (c) 0700–0900 LST, (d) 0900–1100 LST, (e) 1100–1300 LST, and (f) 1300–1500 LST. Rainfall contours are 20-mm intervals starting from 10 mm. The heavy, notched line indicates the frontal position at the middle of the accumulated rainfall period. Terrain contours are 1.5-km intervals.

storm environments observed over the tropical and subtropical oceans (Lucas et al. 1994a).

In the upper levels, a trough moved eastward from northern China to Japan. At 1200 UTC 24 June, the axis of the upper-level trough at the 300-hPa level was located at approximately 128°E, northeast of Taiwan (Fig. 5a). A strong northwesterly flow with a maximum wind speed greater than 40 m s^{-1} was observed on the northeastern periphery of the semipermanent south Asian anticyclone (29°N, 107°E) and behind the traveling upper-level trough. A pronounced upper-level diffluent airflow occurred over the southeastern China coast and the Taiwan area between the northwesterly flow behind the trough and the northeasterly flow on the southeastern quadrant of the south Asian anticyclone. The geopotential height gradients were weak in the diffluent region (Fig. 5b). This region was downstream of the northwesterly jet behind the trough with significant flow deceleration. Ageostrophic winds pointing southwestward across the geopotential contours were observed over the diffluent region (Fig. 5b) due to the inertial-advective effect of the horizontal winds, resulting in upper-level divergence there (Fig. 5c). Uccellini and Johnson (1979) observed upper-level divergence on the left front quadrant of an upper-level jet streak. Our case is slightly different from the classical case documented by Uccellini and Johnson (1979) because the maximum wind speed deceleration downstream of the jet occurred in the upper-level diffluent region. Over this region, the strong northwesterly flow turned sharply into the northeasterly flow along the southeastern China coast. Over the northern China coastal area, the upper-level convergence (Fig. 5c) was caused by the along-stream ageostrophic winds due to the curvature effect (Shapiro and Kennedy 1981; Chen et al. 1994).

Note that the upper-level divergence was observed

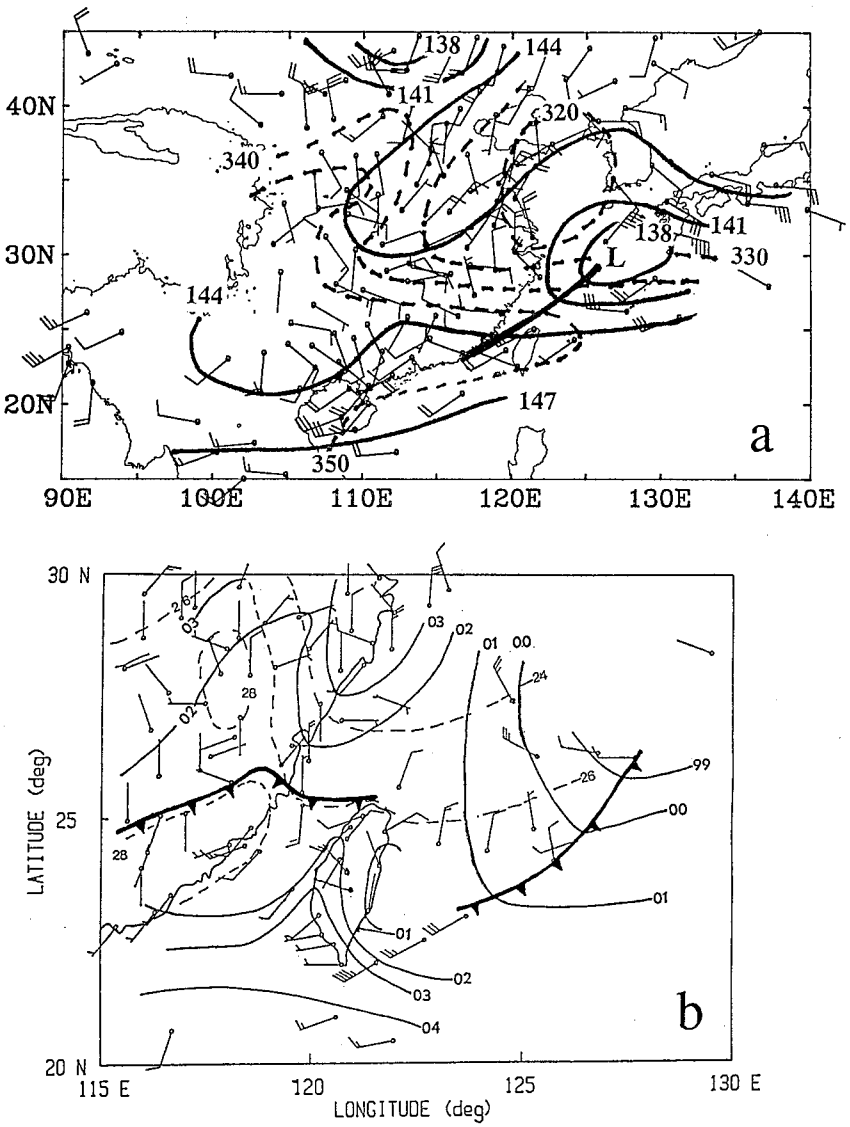

FIG. 3. Synoptic-scale charts analyzed subjectively for 1200 UTC (2000 LST) 24 June 1987. (a) 850 hPa: geopotential heights (solid) every 30 m and equivalent potential temperature (dashed) every 10 K. The heavy line indicates the location of the pressure trough. Terrain contour for 3 km is also plotted. (b) Surface: sea level pressure (solid) every 1 hPa (hectopascals minus 1000) and temperature (dashed) every 2°C. The heavy, notched line indicates the surface frontal position. Winds (m s^{-1}) with full barb and half-barb representing 5 and 2.5 m s^{-1}, respectively.

prior to the development of heavy precipitation over northwestern Taiwan. The upper-level divergence behind a trough is a unique feature for this late season (after the seasonal transition in mid-June 1987) heavy rainfall event and provides an important upper-level support for the development of heavy precipitation over Taiwan. This is different from an early-season case (21–23 May) presented by Chen and Li (1995a). For their case, the upper-level baroclinic forcing is important for the development of heavy rainfall. Even though this is a late season case with weak thermal contrast across the Mei-Yu front, the presence of the upper-level divergence prior to the occurrence of heavy precipitation attests that the secondary circulation across this Mei-Yu front is not driven by a pure CISK process as suggested by Chen and Chang (1980).

At 1500 UTC 24 June, a northeast–southwest-aligned cloud band formed over the northern Taiwan Strait (Fig. 6). It developed beneath the upper-level diffluent airflow (Fig. 5a) and along the axis of the maximum equivalent potential temperature at the 850-hPa level when the low-level wind-shift line associated with the southern portion of the pressure trough moved over the northern Taiwan Strait (Fig. 3a). It was the system that produced heavy

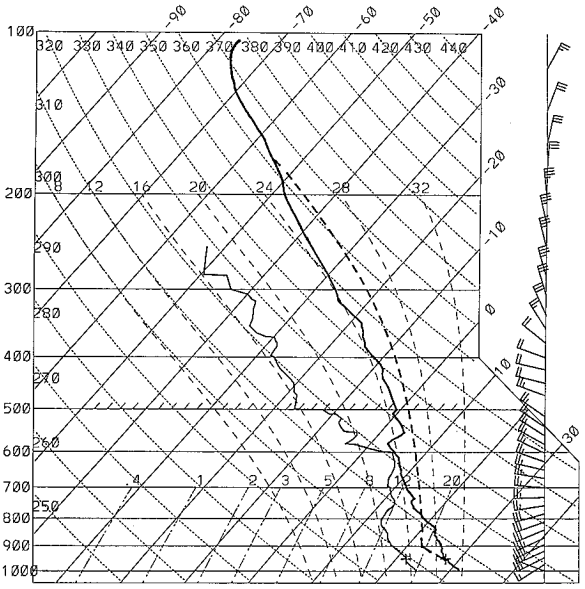

FIG. 4. Sounding for 1200 UTC (2000 LST) 24 June at Penchiao station (46685, 25.00°N, 121.43°E; Fig. 1a). Thermodynamic profiles plotted on skew *T*–log*p* diagram, winds plotted at right with the same convention as in Fig. 3a.

rainfall along the northwestern coast of Taiwan on the morning of 25 June. We will further discuss the mesoscale precipitation features in sections 4–6.

At the surface, the Mei-Yu front over northwestern Taiwan was characterized by the southwesterly flow ahead and the northeasterly flow behind (Fig. 3b). The horizontal temperature contrast across the front was rather weak as compared to the early season (before the seasonal transition in mid-June) cases. The movement of the surface front was retarded by the hilly terrain along the southeastern China coast. The cold air behind the front was ducted around the coast (Fig. 3b). As a result, the low-level wind-shift line associated with the 850-hPa trough moved eastward over northern Taiwan Strait before the surface front arrived (Fig. 3) as found by Chen and Hui (1992) for the 13–14 May case. In their case, however, the atmosphere was extremely dry over the Taiwan Strait with large-scale sinking motion, and little precipitation was observed over the Taiwan area. As the surface front moved over Taiwan, it was split into two branches by the central mountain range (Fig. 3b). The eastern part of the front moved faster than the western one, which is a typical feature of the frontal translation over Taiwan (Wang 1986). The western portion of the front passed over the CP4 radar site around 1300 LST 25 June (Parsons and Trier 1990). The mean speed for the western branch of the front was about 2.6 m s^{-1} during 0200–0500 LST 25 June over northwestern Taiwan and decreased to about 1.1 m s^{-1} during 1100–1400 LST.

c. The barrier jet along the northwestern coast of Taiwan

From aircraft observations during 21–22 May 1987 (TAMEX IOP 3), Chen and Li (1995a) observed strong low-level winds along the northwestern Taiwan coast in the prefrontal atmosphere as a result of the interaction between the southwesterly monsoon flow and the island obstacle. The locally strong coastal wind is referred to as a barrier jet. In this section, surface mesonet data, soundings, and the VAD winds at the CAA and NCAR radars are used to construct the low-level airflow pattern over the Taiwan area. We will show that the barrier jet is also present for this case. It was completely ignored in the previous studies (Lin et al. 1989, 1992; Jou and Deng 1992).

At 1800 UTC 24 June (0200 LST 25 June), the western portion of the surface front arrived in northwestern Taiwan (Fig. 7a). A pronounced surface pressure ridge was evident on the windward side along the southwestern and western coasts (Fig. 7a). The southwesterly flow split offshore of the southwestern coast and moved around the island. In the prefrontal atmosphere, strong winds were observed in the layer of 0.5–1.5 km along the northwestern coast with the maximum wind speed greater than 20 m s^{-1} (Figs. 7b–d).

To further show the presence of the barrier jet, we compared the wind profile over northwestern Taiwan with the upstream southwesterly flow. Station 46810 (20.70°N, 116.72°E, Fig. 1a) is located approximately 400 km upstream of the southwestern coast of the island. The upstream wind profile exhibited the low-level southwesterly monsoon flow with a wind speed of about 13 m s^{-1} at 1.5 km (Fig. 8). The winds veered from 210° at the surface to 245° at 3 km, suggesting low-level warm advection in the prefrontal atmosphere. Compared with the upstream flow, the wind speed at the NCAR CP4 radar site along the northwestern coast was significantly greater below 3 km (Fig. 8), the approximate ridge top of the central mountain range. The maximum wind speed at the radar site was about 22 m s^{-1} at 1.0 km, which was about twice the upstream wind speed. The substantial increase of the low-level wind speed over northwestern Taiwan was associated with the flow acceleration down the pressure gradient (Fig. 7a) as found by Chen and Li (1995a). It is apparent that the strong coastal wind is different from the strong subsynoptic-scale prefrontal southwesterly monsoon flow (or LLJ) defined by Chen and Yu (1988).

4. Radar echo patterns

During the heavy rain episode, the western portion of the surface front propagated southward along the northwestern coast, and the northeast–southwest-aligned wind-shift line associated with the pressure trough moved eastward toward the coast. In previous studies (i.e., Lin et al. 1989, 1992; Jou and Deng 1992),

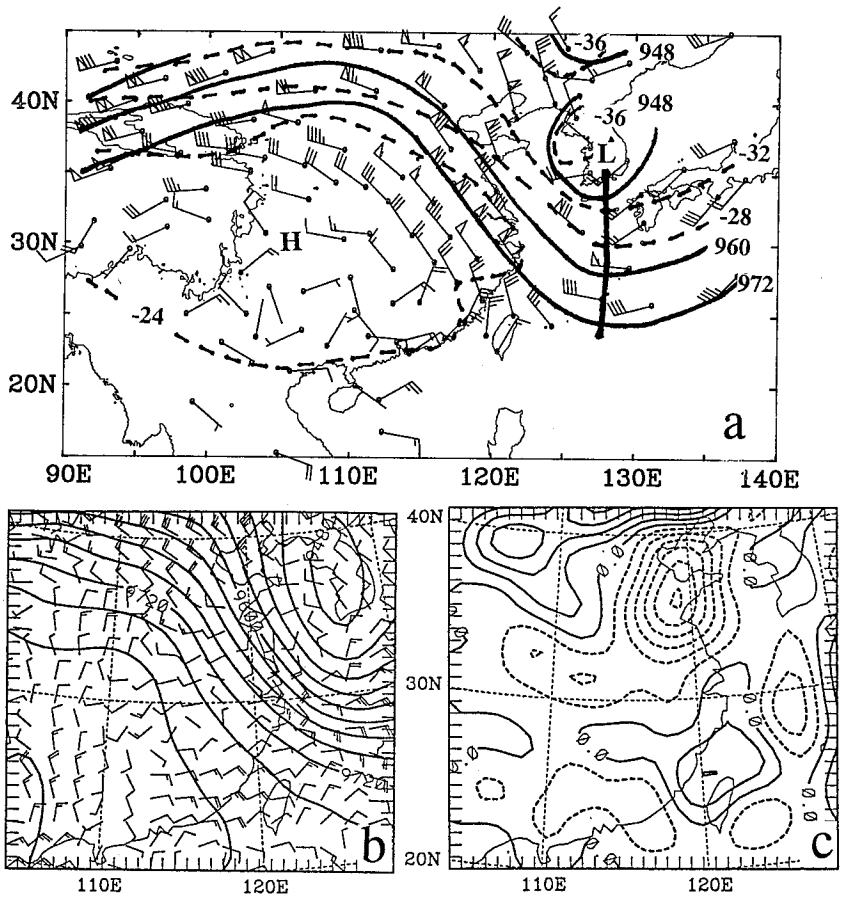

FIG. 5. Synoptic-scale maps analyzed (a) subjectively and [(b) and (c)] objectively at the 300-hPa level for 1200 UTC (2000 LST) 24 June 1987. (a) Geopotential heights (solid) every 120 m and isotherms (dashed) every 4°C. The heavy line in (a) indicates the trough position. Terrain contour for 3 km is also plotted. (b) Ageostrophic winds and geopotential heights (every 30 m) and (c) divergence field (every 1.0×10^{-5} s^{-1}). Winds (m s^{-1}) with one pennant, full barb and half barb represent 25, 5, and 2.5 m s^{-1}, respectively. The solid and dashed lines in (c) represent positive and negative values, respectively.

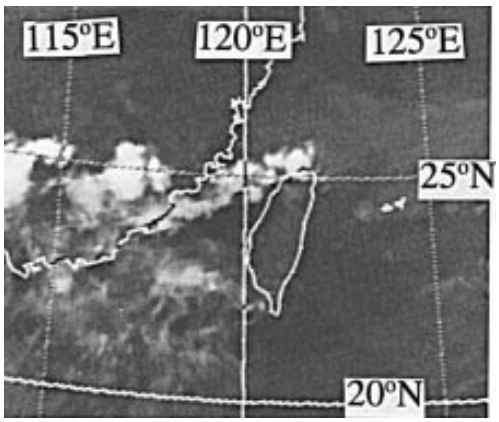

FIG. 6. Infrared satellite image for 1500 UTC (2300 LST) 24 June 1987.

no distinction was made between this wind-shift line and the Mei-Yu front. In this section, we will use Doppler radar data to distinguish the surface front and the low-level wind-shift line. We will show that the most intense convection is associated with the low-level wind-shift line. In addition, a convective line associated with the land-breeze front is also discussed.

a. Convection along the Mei-Yu front

The distribution of the radial velocity at the 0.5-km level obtained from CAA radar for 0220 LST shows a zero isotach line to the north of the radar site (Fig. 9). Since the Mei-Yu front was characterized by a low-level wind shift from southwesterly to northeasterly flow, this line represented the approximate location of the surface front over northwestern Taiwan at this time. The positive radial velocities (away from the radar) south of the front represented the prefrontal southwesterlies, whereas the

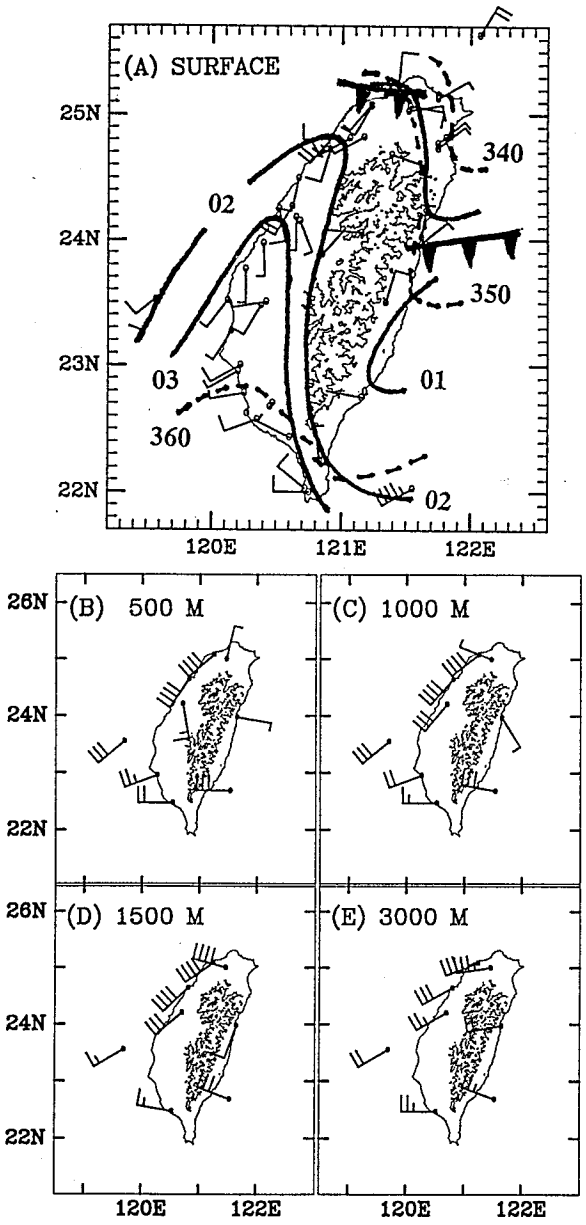

FIG. 7. (a) Surface subjective analysis of sea level pressure (solid) every 1 hPa (hectopascals minus 1000) and the equivalent potential temperature (dashed) every 10 K for 0200 LST 25 June. (b)–(e) Low-level wind fields for various levels constructed from rawinsonde, pibal, and VAD winds at CAA (25.08°N, 121.21°E) and CP4 radar (24.64°N, 120.76°E). Wind plotting convention same as Fig. 3a and the terrain contours every 1.5 km.

negative radial velocities (toward the radar) behind the front indicated the postfrontal northeasterlies. The frontal position determined from radial velocity is generally consistent with the surface analysis over northwestern Taiwan at this time (Fig. 7a; Fig. 17 in Chen 1991). The sounding for station 46685 (25.0°N, 121.4°E; Fig. 1a) and the VAD wind profiles for CP4 radar site show that the depth of the postfrontal northeasterlies was about 0.5–0.8 km.

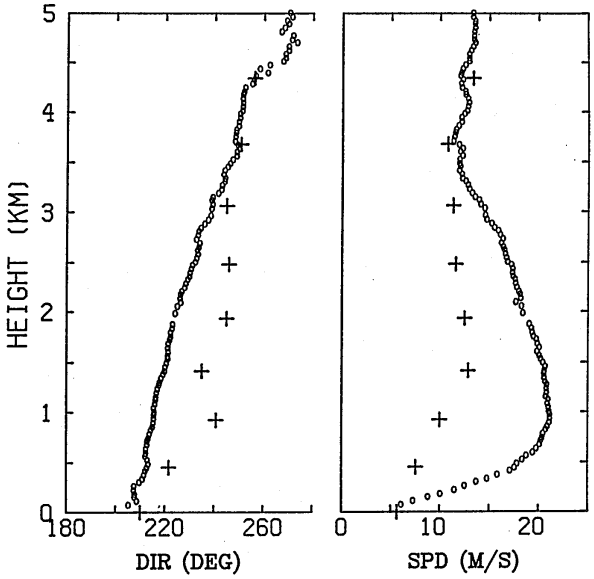

FIG. 8. Vertical profiles of (a) wind direction and (b) speed at 0200 LST 25 June for Tungsha Tao station (46810; 20.70°N, 116.72°E) (+) and the CP4 radar site (24.64°N, 120.76°E) (○).

Figure 10 shows a north–south vertical cross section (normal to the surface front) of the reflectivity and the system-relative wind fields for 0220 LST. The winds are obtained from the single Doppler analysis based on the assumption that the front had a quasi-two-dimensional

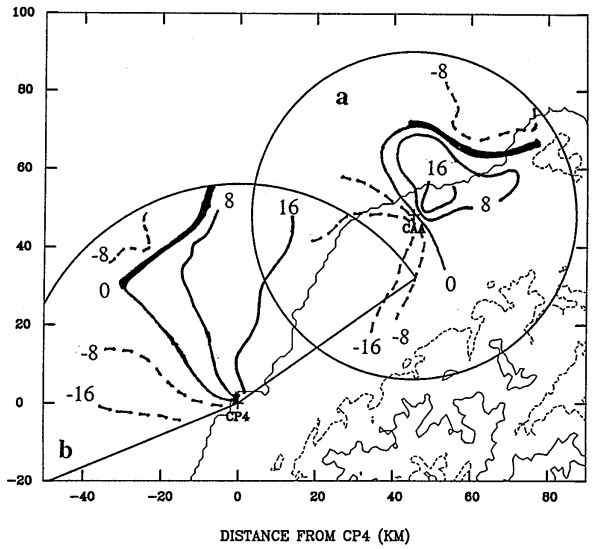

FIG. 9. Distribution of radial velocity at the 0.5-km level for 0220 LST 25 June. Contours are 8 m s^{-1}. The heavy lines in circle a and sector b denote the positions of the front and the wind-shift line, respectively. Circle a and sector b are the largest areas of the available data at the 0.5-km level interpolated by the bilinear method with the maximum acceptable distance of 1 km along the radar beams. Abscissa and ordinate labels denote distances (km) east and north of CP4 radar. Radar positions (+) and the terrain contours every 0.5 km are also shown.

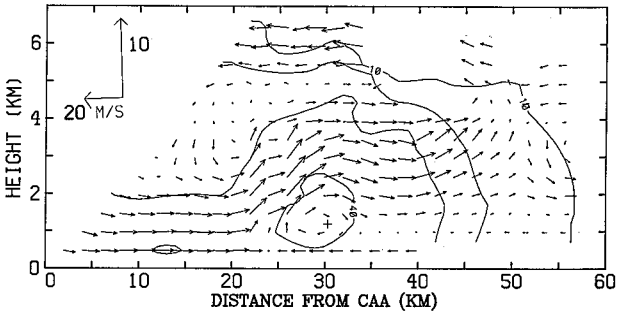

FIG. 10. North–south vertical cross section of reflectivity (10-dBZ intervals starting from 10 dBZ) and system-relative winds obtained from the single-Doppler analysis. The scales for winds are given in the upper left side of the figure. Distances are in kilometers from the CAA radar to the north.

structure (Browning and Harrold 1970). The horizontal wind components on the cross section are calculated from the CAA Doppler velocities, and the radar geometry and the vertical velocities are estimated by integrating the quasi-two-dimensional, anelastic continuity equation. The leading edge of the front was located about 25 km north of the CAA radar at this time (Fig. 10). In the lowest levels, the air from the south met the northerly flow in the lowest levels at the leading edge and rose toward the rear with upward motion leaning back over the shallow northerly flow. Behind the surface front, there was a rear-to-front relative flow near the surface with a front-to-rear return aloft. The relative flow pattern is similar to that found in other TAMEX cases (Chen and Hui 1990; Trier et al. 1990). A region with high reflectivity ($\geq$40 dBZ) was found just behind the surface front in the lowest 3 km with echo tops ($\sim$10 dBZ) about 6 km (Fig. 10).

b. Rainband along the low-level wind-shift line

The radial velocities from the CP4 radar at the 0.5-km level for 0220 LST 25 June show a northeast–southwest-aligned, zero radial velocity line approximately 45 km northwest of the radar site (Fig. 9). The winds were from the southwest ahead of the zero isotach line and had a notable component toward the radar behind the line. This zero radial velocity line was observed at the lowest elevation angles ($\leq$3.3°). It represents the low-level wind-shift line associated with the pressure trough over the Taiwan Strait shown by the 850-hPa synoptic map (Fig. 3a).

Vertical cross sections of reflectivity and radial velocity were obtained through range–height indicator (RHI) scans from the CP4 radar at 0240 LST 25 June. The RHI scan along 335° azimuth is almost normal to the wind-shift line. A distinct wind-shift zone with a depth of about 3 km was observed 40 km northwest of the radar site (Fig. 11a). The wind-shift line was much deeper than the Mei-Yu front. There were high reflectivities located around the wind-shift line (Fig. 11b). The convection associated with the wind-shift line was deep with echo tops ($\sim$10 dBZ) around 15 km. The echo tops were much higher than those associated with the Mei-Yu front. As suggested by Jou and Deng (1992) and Lin et al. (1992), in regions with well-developed echoes, the wind-shift line was modified by downdrafts. It will be shown later that this modification was most significant on the northeastern part of the rainband as the echoes moved from southwestern portion of the rainband toward the northeast and matured.

Based on the evolution of the radial velocities from the low elevation angles of the CP4 radar, the wind-shift line moved southeastward toward the northwestern coast. The mean speed of this line was about 3.9 m s^{-1} between 0220 and 0320 LST, decreasing to about 2.5 m s^{-1} in the next few hours as it moved toward the coast. This wind-shift line passed the CP4 radar site around 0730 LST, about 6 h before the frontal passage. Apparently, the northeast–southwest-aligned wind-shift line and the Mei-Yu front are two distinct features with different horizontal orientation, depth, and movement. The convective activities associated with them also exhibited different characteristics. Note that this wind-shift line is not the gust front caused by the deep convection in the frontal zone. As will be discussed later, on the southwestern tip of the rainband, new convective elements were continuously generated along this wind-shift line and merged with the echoes associated with the rainband as they moved northeastward.

c. Convection associated with the land-breeze front

Figure 12 presents the hodograph of the surface winds during 24 June 1987 for tower station TXE15 (24.49°N, 120.67°E; Fig. 1a) at the northwestern Taiwan coast. The average wind during the day (the heavy line in Fig. 12) at this station was parallel to the coastline from the southwest. Under the prefrontal southwesterly flow regime, the land–sea breeze components (deviations from the daily-averaged resultant wind, the light line in Fig. 12) were evident at this station. During the nighttime, the offshore flow components had a maximum value of approximately 3 m s^{-1} (Fig. 12). The surface winds for stations along the western coast also exhibited an offshore wind component at 0200 LST 25 June (Fig. 7a).

The land-breeze front and the echo pattern associated with it were determined from a series of RHI scans obtained from the CP4 radar around 0240 LST 25 June. The RHI scan along 305° azimuth is almost normal to the daily averaged surface resultant wind vector (Fig. 12). It shows that positive radial velocities (away from the radar) were very shallow ($\leq$0.5 km) within a range of 15 km from the radar site (Fig. 11c). The shallow positive radial velocities represent the land breezes. The land breezes can be also identified from other RHI scans. Along 335° azimuth (Fig. 11a), the southwesterly flow had a wind component away from the radar. In the lowest 0.5 km, the large positive radial velocities within the

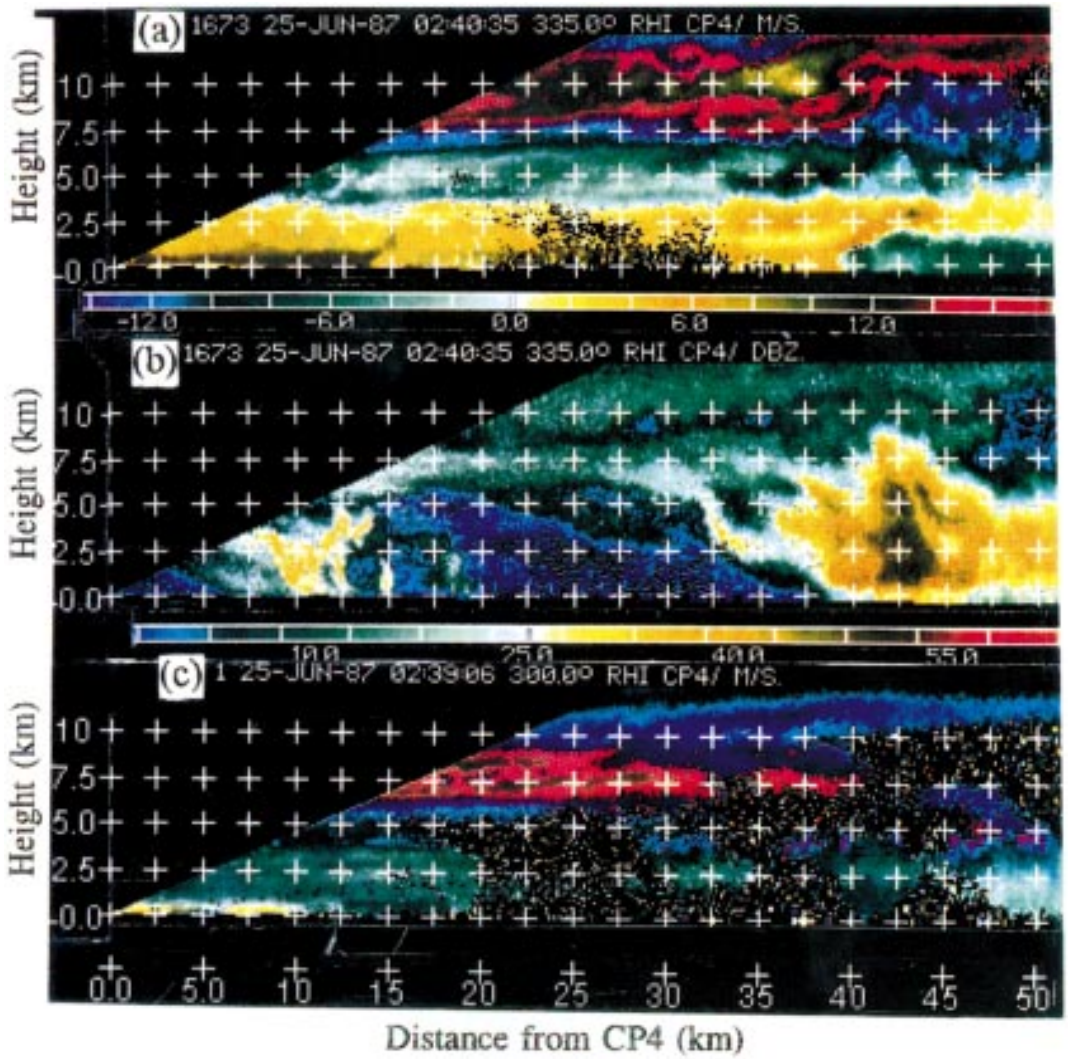

FIG. 11. Vertical cross sections (RHI scans) obtained from the CP4 radar at 0240 LST 25 June 1987. (a) Radial velocity and (b) reflectivity along 335° azimuth; (c) radial velocity along 300° azimuth. Distances are in kilometers from the CP4 radar to the northwest (right-hand side of the figure). Scales for radial velocity and reflectivity are given at the bottom of (a) and (b), respectively.

radar range of 10–15 km represented the superposition of the land breezes with the low-level southwesterly flow (Fig. 11a). There was an echo maximum associated with the land-breeze front (Fig. 11b). The echo tops associated with the land-breeze front were lower ($\leq$5 km) than those associated with the northeast–southwest-aligned wind-shift line.

5. Evolution of the rainband

In the previous sections, our analysis shows that the convection associated with the rainband was more intense and deeper than that associated with the surface front and the land-breeze front. In this section, the evolution of the rainband associated with the low-level wind-shift line is analyzed. We will show that there were some long-lived reflectivity maxima embedded in the rainband. These reflectivity maxima prolonged the lifetime of the rainband and produced persistent heavy rainfall along the northwestern coast as they moved toward the coast.

The evolution of the reflectivity field at the 2.5-km level during the heavy rain episode is presented in Fig. 13. The positions for the Mei-Yu front and the low-level wind-shift line between the barrier jet along the western Taiwan coast and the westerly flow coming off the southeastern China coast behind the pressure trough are superimposed. The frontal location is determined from both the surface analysis and the zero isotach line observed from the low elevation scans of the CAA radar. The wind-shift line is based on the zero isotach line or the maximum shear of the radial velocity observed by both the CP4 and CAA radars. At 0120 LST, three types of echoes were identified (Fig. 13a). One was located near the surface front north of the CAA radar site. Another was a northeast–southwest-oriented, prefrontal

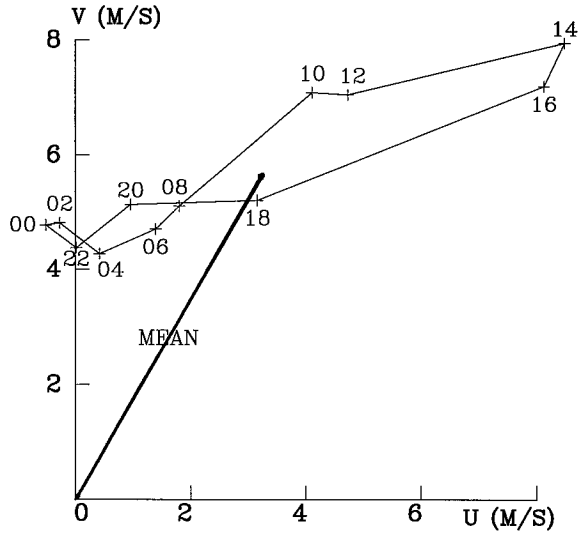

FIG. 12. Hodograph of the surface winds for station TXE15 (24.49°N, 120.67°E; Fig. 1a) on 24 June 1987. The heavy line indicates the mean wind during that day. The numbers denote the time (LST).

rainband associated with the wind-shift line over the Taiwan Strait northwest of the CP4 radar site. The third was a convective line associated with the land-breeze front offshore of the northwestern coast. In the following hours, the rainband moved southeastward toward the northwestern coast with the wind-shift line (Fig. 13a–d). The surface front moved slowly southward, while the convective line associated with the land-breeze front was almost stationary (Figs. 13a,b). The motion for the rainband was relatively uniform before the northeastern portion of the rainband moved inland. The mean motion was about 3.8 m s^{-1} from 332°. After the rainband moved into the coastal region, the speed for the northeastern portion of the rainband reduced significantly (Figs. 13c,d).

During the analysis period, the most intense and the deepest echoes were located along the wind-shift line in the prefrontal atmosphere. Based on aircraft and sounding observations for a TAMEX frontal case (13–14 May 1987), Chen and Hui (1992) found that as the surface front moved southward over the Taiwan Strait, the northwesterly flow coming off the southeastern China coast behind the 850-hPa trough was undercut by the postfrontal shallow northeasterlies (their Figs. 24 and 25). Similar to the 13–14 May case, the wind-shift line associated with the 850-hPa trough in our case was undercut by the postfrontal northeasterlies as the surface front arrived in northwestern Taiwan. As a result, the echoes associated with the wind-shift line were rather weak in the postfrontal region (Fig. 13). At 0120 LST, the convection at the intersection between the wind-shift line and the surface front was enhanced (Fig. 13a). The convection on the northeastern part of the rainband weakened and dissipated rapidly as it moved inland. The weakening and dissipation of the reflectivity maxima on the northeastern part of the rainband may be related to the orientation of the rainband and the development of the sinking motion beneath the anvils on the warm, moist side of the wind-shift line (section 6c). The low-level inflow of the warm, moist air from the front was partly blocked by the reflectivity maxima developing on the southwestern part of the rainband and the development of sinking motion on the southeastern side of the reflectivity maxima. At 0730 LST, a secondary line of echoes was found behind the wind-shift line (Fig. 13d). The echoes associated with this line were weaker than those associated with the rainband.

Figure 13 also reveals that there were several reflectivity maxima embedded in the rainband. Some of these reflectivity maxima were short-lived (about a half hour) and had small horizontal scales. Some lasted longer (>2 h). To study these long-lived reflectivity maxima, we analyze the high-time-resolution (~5–10 min) reflectivity data obtained from the CP4 radar during 0120–0800 LST. In this study, these long-lived reflectivity maximum areas are tracked if they have 1) a lifetime greater than 2 h, 2) a closed reflectivity contour at least 3 dBZ greater than its surroundings, and 3) the maximum horizontal extent of the reflectivity core ($Z \geq 40$ dBZ) during the lifetime greater than 10^2 km.

It is found that these reflectivity maxima always formed on the southwestern tip of the rainband over the ocean. They were generated along the low-level wind-shift line (Fig. 13). Once formed, these reflectivity maxima developed rapidly and merged with the main body of the rainband (≥30 dBZ) from the southwest. The reflectivity generally intensified on the southeastern side of the reflectivity maxima and weakened on the western/northwestern corner, resulting in the east-southeastward movement of these maxima. These reflectivity maxima often have several small individual cells with much shorter lifetimes. During the lifetime of a long-lived reflectivity maximum, short-lived cells along the rainband were also found to blend into the reflectivity maximum region. Occasionally, some short-lived cells developed south of the rainband. These small cells were advected northeastward by the low-level southwesterly flow ahead of the rainband and merged with the reflectivity maxima embedded in the rainband as found by Lin et al. (1992).

The reflectivity maxima embedded in the rainband moved east-southeastward with a speed of 5–10 m s^{-1} before they arrived at the northwestern coast. Their movement relative to the rainband was from the southwest to the northeast (Fig. 14). The mean environmental wind (V_m) ahead of the rainband and the mean motion of the rainband (V_b) are given in the lower left corner of Fig. 14. The mean environmental wind was about 7.3 m s^{-1} from 274° with the vertical shear of 2.4×10^{-3} s^{-1}, which was calculated by the density-weighted mean in the layer 0.5–10.0 km from the sounding data for station 46734 (23.55°N, 119.62°E; Fig. 1a) during

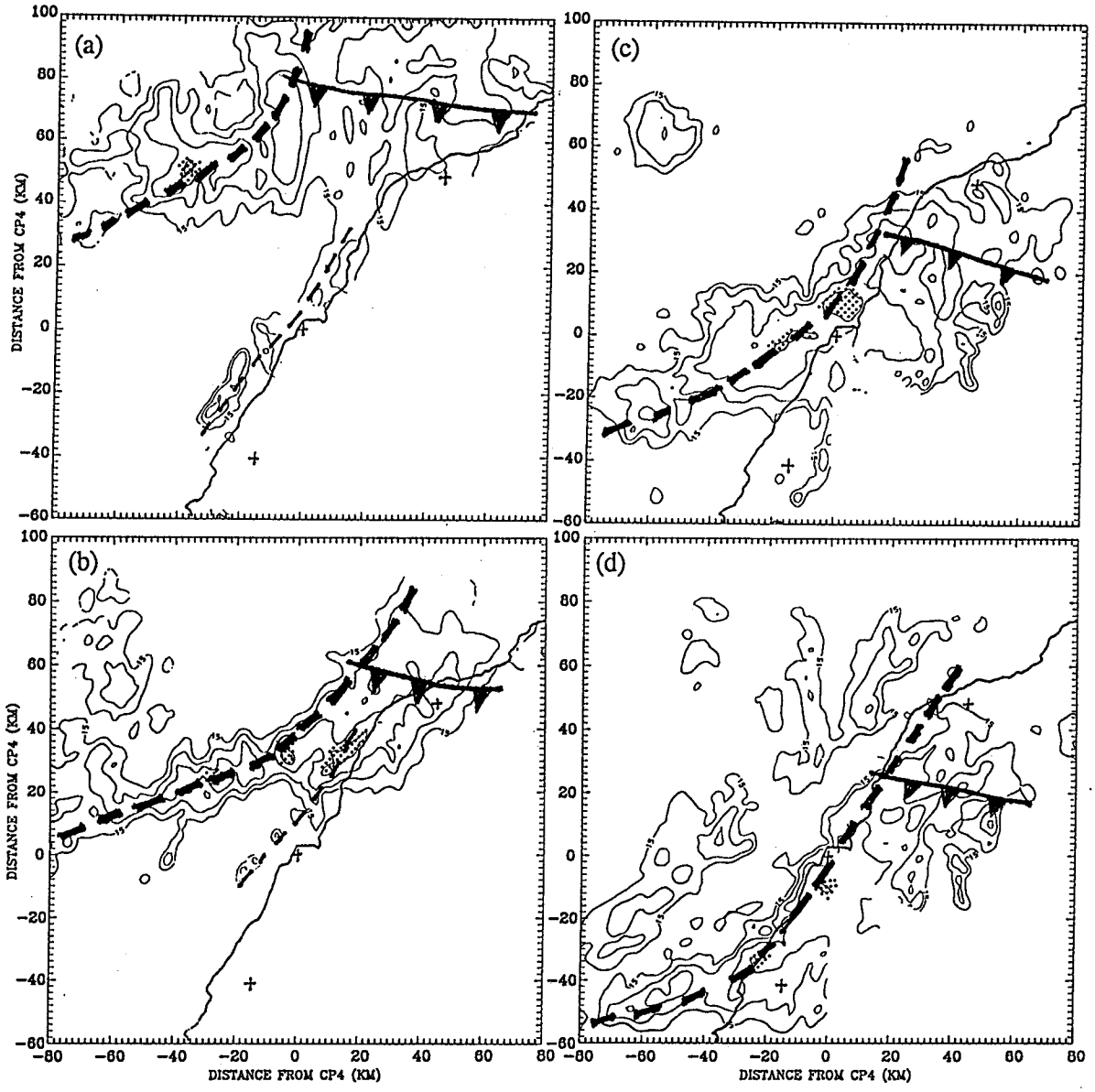

FIG. 13. Horizontal distributions of reflectivity (dBZ) obtained from the CP4 radar for (a) 0120 LST, (b) 0320 LST, (c) 0525 LST, and (d) 0730 LST 25 June at the 2.5-km level. The solid, the heavy-dashed, and the dashed lines indicate the approximate positions for the surface front, the low-level wind-shift line, and the land-breeze front, respectively. Reflectivity contours are 10-dBZ intervals with values greater than 45 dBZ shaded. Distances are in kilometers from the CP4 radar. Radar positions (+) and the northwestern coastline of Taiwan are also given.

0200–0500 LST 25 June. The speeds of the reflectivity maxima were about the same as the mean environmental flow, whereas the directions of the reflectivity maxima movement generally deviated about 10°–30° to the right of the mean wind vector.

The peak reflectivity for each reflectivity maximum is plotted as a function of time (Fig. 15a) and as a function of the distance normal to the coastline (Fig. 15b). The intensity for the reflectivity maxima increased quickly during the early stage (Fig. 15a) as they moved along the wind-shift line toward the coast. They reached the maximum intensity near the coast (Fig. 15b). Reflectivity maximum A was first identified at 0120 LST. The reflectivities associated with reflectivity maximum A increased during its movement to the coast. It moved to the northeastern end of the rainband around 0300 LST (Fig. 14). At this time, its maximum reflectivity began to decrease (Fig. 15a) as it reached the late stage of its life cycle. About a half hour later, reflectivity maximum A moved to 13 km offshore of the coast and its intensity increased again (Fig. 15b). Reflectivity maximum A finally reached the maximum intensity over

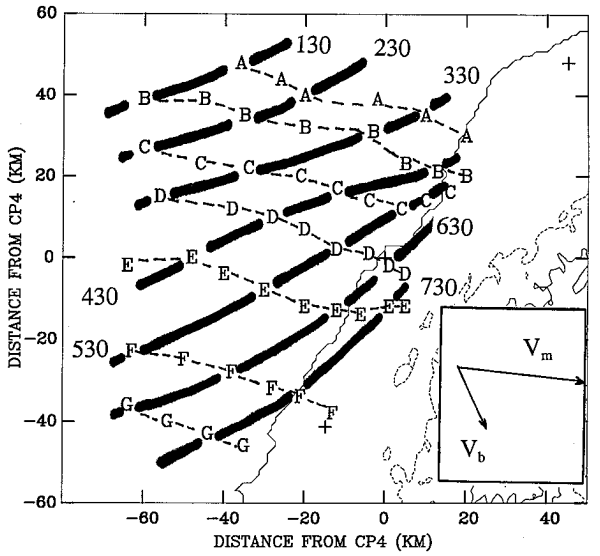

FIG. 14. Evolution of the long-lived reflectivity maxima (A–G) embedded in the rainband during 0130–0800 LST 25 June. The solid and dashed lines indicate the positions for the rainband and the tracks for the reflectivity maxima, respectively. The numbers denote the time (LST). Distances are in kilometers from the CP4 radar. Radar positions are denoted by (+) and terrain contours are every 0.5 km. The vectors in the lower right corner denote the mean motion of the rainband (V_b) and the density-weighted mean wind (V_m) in the layer 0.5–10.0 km during 0200–0500 LST 25 June for station 46734 (23.55°N, 119.62°E; Fig. 1a).

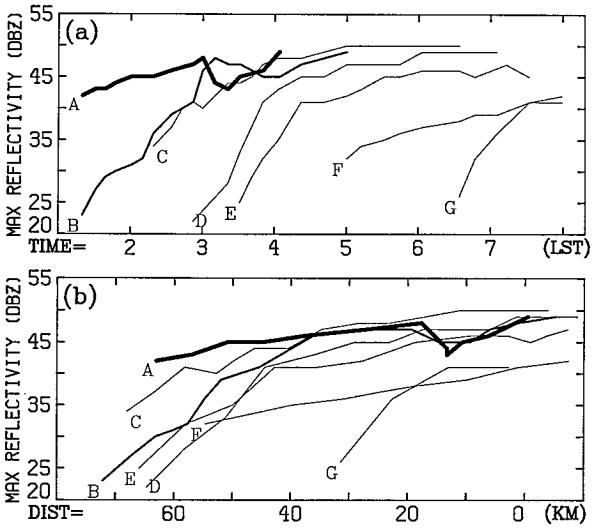

FIG. 15. (a) Time series of the peak reflectivities for the long-lived reflectivity maxima (A–G) during 0120–0800 LST 25 June 1987; (b) the peak reflectivities as a function of the distance (km) normal to the northwestern coast.

the coastal region. The peak reflectivity of maximum B experienced a similar trend as maximum A (Fig. 15). The second increase of the intensity for both reflectivity maxima A and B was related to their merger with the convective line offshore of the coast. It appears that these reflectivity maxima were enhanced by the convective line offshore. The intensity for other reflectivity maxima (C–G) increased gradually as they moved toward the coast. Reflectivity maxima C–G were generated closer to the coast than reflectivity maxima A and B, and intensified as they moved toward the coast. There was no second increase in the intensity of C–G because the convective line associated with the land-breeze front was absent as they moved close to the coastline after sunrise. After they moved inland, they weakened and disappeared rapidly.

In summary, there were several long-lived reflectivity maxima embedded in the rainband. These reflectivity maxima formed on the southwestern tip of the rainband and along the wind-shift line associated with the 850-hPa pressure trough. They merged with the rainband from the southwest and continued to move from southwest to northeast along the rainband. The reflectivity maxima on the northeastern part of the rainband dissipated rapidly after they moved inland. The rainband, as a whole, moved southeastward with the low-level wind-shift line and slowed down after it moved into the coastal region. The continuous generation of new reflectivity maxima on the southwestern part of the rainband and their movement from southwest to northeast along the rainband are important to prolong the lifetime of the rainband. These long-lived reflectivity maxima moved into northwestern Taiwan and resulted in persistent heavy rainfall along the northwestern coast. In the postfrontal region, the wind-shift line was undercut by the shallow northeasterlies. Weak and shallow echoes were observed behind the surface front.

6. Dual-Doppler analysis of the rainband

During 0220–0420 LST, the rainband moved close to the northwestern Taiwan coast (Fig. 13b) and was located within the dual-Doppler lobe of the CAA and CP4 radars. To study the mesoscale airflow and the rainband structure, we performed dual-Doppler analysis during this period.

a. Horizontal views

Figure 16 shows the low-level horizontal wind (relative to ground), reflectivity, and divergence fields at the 1.5-km level for 0250 LST. The most prominent feature in the low-level airflow associated with the rainband was the barrier jet converging with the westerly flow coming off the China coast behind the wind-shift line. At the 1.5-km level, strong southwesterly flow prevailed ahead (southeast side of the figure) of the rainband with the maximum wind speed greater than 20 m s^{-1} (the barrier jet) along the northwestern coast. Behind the rainband, winds generally were from the west (Fig. 16a). A pronounced convergence zone was found between the barrier jet and the westerlies (Fig. 16b). The maximum convergence associated with the wind-shift

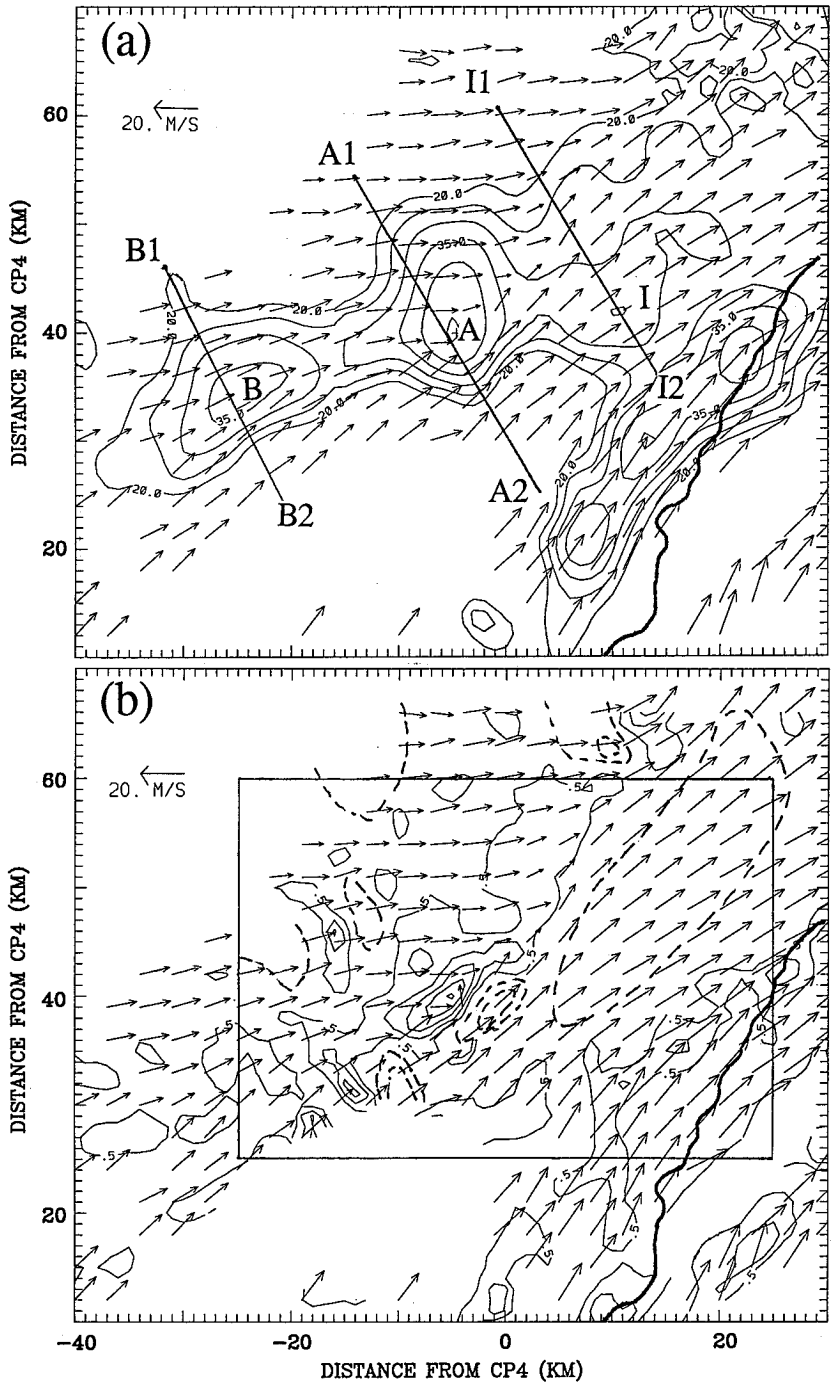

FIG. 16. Horizontal distributions of (a) reflectivity, (b) convergence, and (c) vertical velocity at the 1.5-km level for 0250 LST 25 June 1987. The horizontal winds (relative to the ground) are overlaid upon each field. The scale for winds is given in the upper left side of each figure. Reflectivity contours are 5-dBZ intervals starting from 20 dBZ. Contours for convergence (solid lines) and divergence (dashed lines) are 1.0×10^{-3} s^{-1} intervals. Vertical velocity is plotted within the box area of (b). Contours for downward (dashed lines) and upward (solid lines) motion are 1 m s^{-1} intervals. Distances are in kilometers from the CP4 radar. The northwestern coastline is also given.

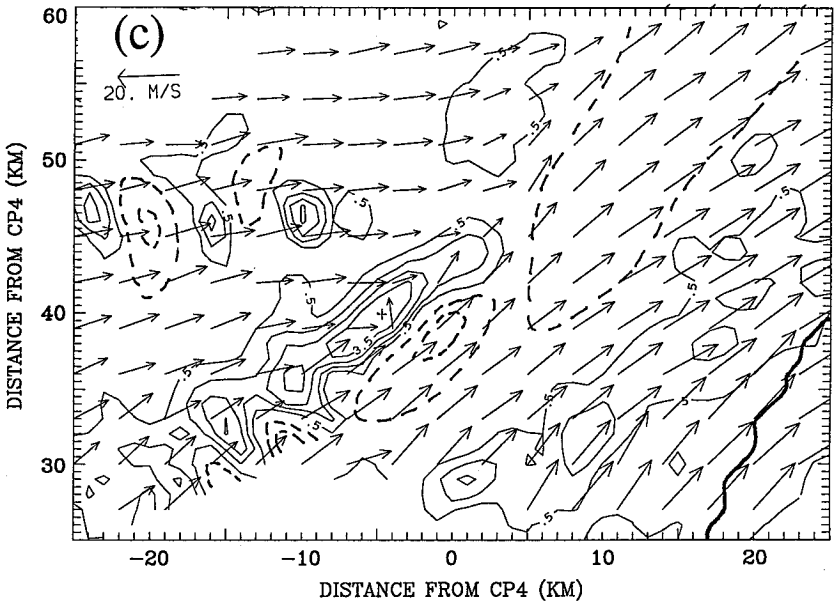

FIG. 16. (*Continued*)

line was about 3.9×10^{-3} s^{-1}. Weak low-level convergence ($\sim 1.6 \times 10^{-3}$ s^{-1}) was observed along the line of convection associated with the land-breeze front (Fig. 16b). Most of the rainband coincided with the low-level northeast–southwest-aligned wind-shift line (Fig. 16a) except the northeastern portion of the rainband, where the echo maximum was located southeast of the convergence zone associated with the wind-shift line. Note that the reflectivity maximum on the northeastern part of the rainband was in the late stage of its life cycle (Fig. 15).

The vertical velocity distribution at the 1.5-km level shows two upward motion regions (Fig. 16c). One occurred along the low-level convergence zone associated with the rainband. Another was located along the convective line associated with the land-breeze front. The strongest upward velocity (~ 4.5 m s^{-1}) was associated with reflectivity maximum A (at about $x = -5$ km, $y = 40$ km; Fig. 16c). The downward motion mainly occurred on the southeastern side of the upward motion zone with a maximum value of 2.5 m s^{-1} at this level. Low-level divergence (Fig. 16b) and sinking motion (Fig. 16c) associated with the echo maximum on the northeastern portion of the rainband were observed southeast of the wind-shift line.

A similar low-level flow pattern with a convergence zone between the barrier jet and the westerly flow was found up to ~ 3 km. Analysis of the low-level flow associated with the rainband during 0220–0420 LST shows that this deep convergence zone was persistent during the analysis period. These results suggest that the low-level convergence between the orographically induced barrier jet and the westerly flow coming off the southeastern China coast behind the wind-shift line played an important role for the maintenance of the rainband. In these previous studies, the low-level wind-shift line and the locally strong coastal winds were viewed as the Mei-Yu front and the subsynoptic-scale low-level jet (LLJ), respectively.

The echo maximum on the northeastern portion of the rainband was referred as to system I by Jou and Deng (1992). Their vertical motion pattern associated with this system (their Fig. 6) is similar to ours (Fig. 16c). Based on analysis of two volume scans at 0653 and 0700 LST, Lin et al. (1992) also observed strong ascending motion northwest of a reflectivity maximum with sinking motion associated with the maximum in the low levels (their Figs. 21 and 22). The reflectivity maximum they analyzed is system E in our study. During 0653–0700 LST, reflectivity maximum E was located on the northeastern portion of the rainband (Fig. 14) and was at the late stage of its life cycle (Fig. 15a). As will be shown in section 6b, the vertical motion patterns were quite different for the reflectivity maxima at different stages during their lifetime. The downward motion dominating over the maximum echo region is a characteristic during the late stage of a reflectivity maximum on the northeastern portion of the rainband. Lin et al. (1992) suggested that the storm outflow in the low levels interacted with the southwesterly flow to form a gust front ahead of the rainband and to generate new cells along the gust front. The cells generated along the gust front were short-lived and less intense compared with the major, long-lived reflectivity maxima embedded in the deep convergence zone. The most intense reflectivity maxima within the rainband were located in the low-level, deep (~ 3 km) convergence zone associated with the wind-shift line.

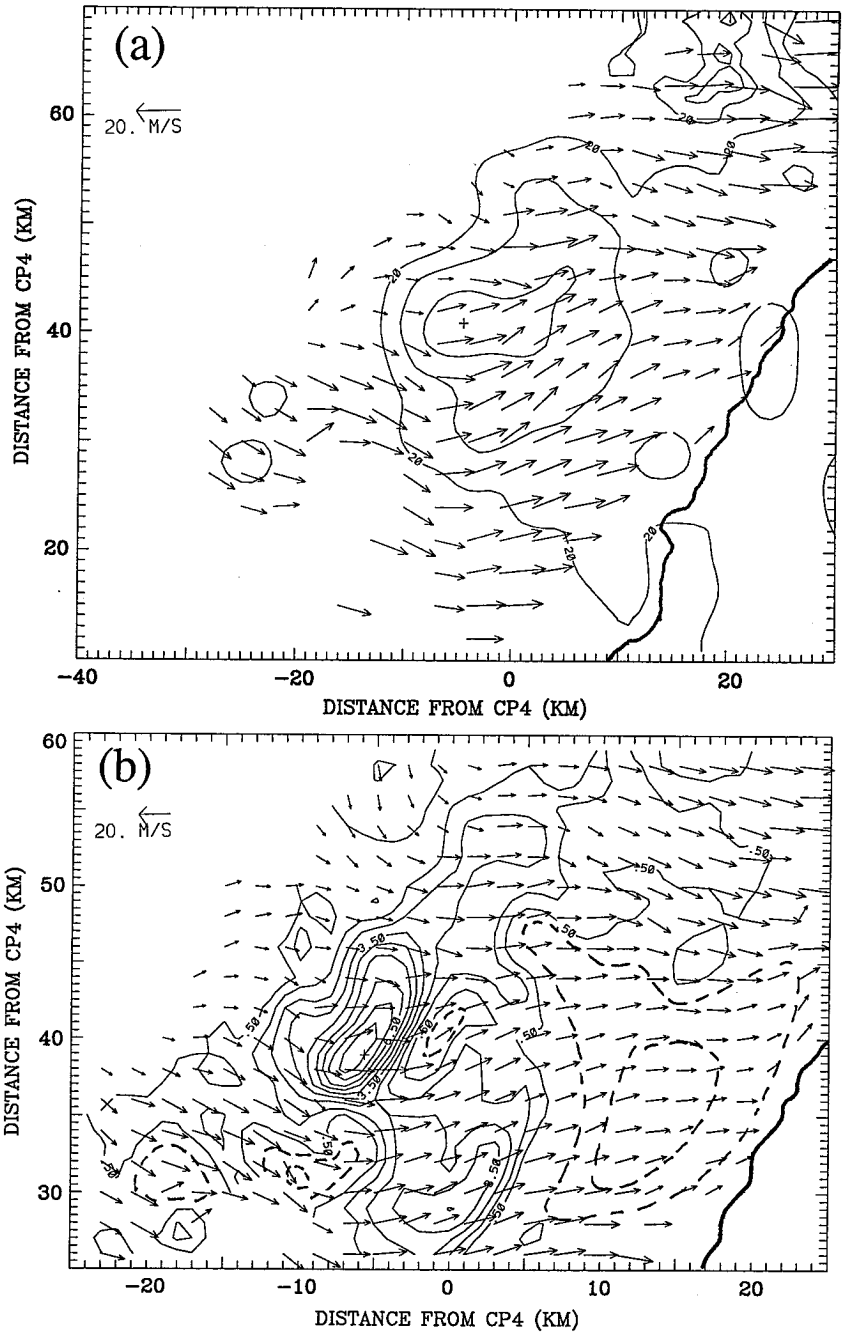

FIG. 17. Horizontal distributions of (a) reflectivity and (b) vertical velocity at the 6.5-km level for 0250 LST. Plotting conventions same as in Figs. 16a and 16c except for reflectivity contours in 10-dBZ intervals.

At the 6.5-km level, the westerly flow dominated (Fig. 17a). The strongest upward motion occurred over the region of reflectivity maximum A with a maximum vertical velocity of 9 m s^{-1} at the 6.5-km level (Fig. 17b). The descending motion mainly occurred ahead (southeast) of the rainband. The downward vertical velocity (<2 m s^{-1}) at this level was much weaker than the ascending motion.

In the upper troposphere, the flow gradually turned to northerlies at the 10.5-km level (Fig. 18), consistent with the wind profile observed over northwestern Taiwan (Fig. 4). The prevailing winds turned clockwise with respect to height, indicating warm advection. The upper-level flow appeared to have a tendency to move around the intense echoes with weak winds on the upwind side. At the 10.5-km level, diffluent airflow was

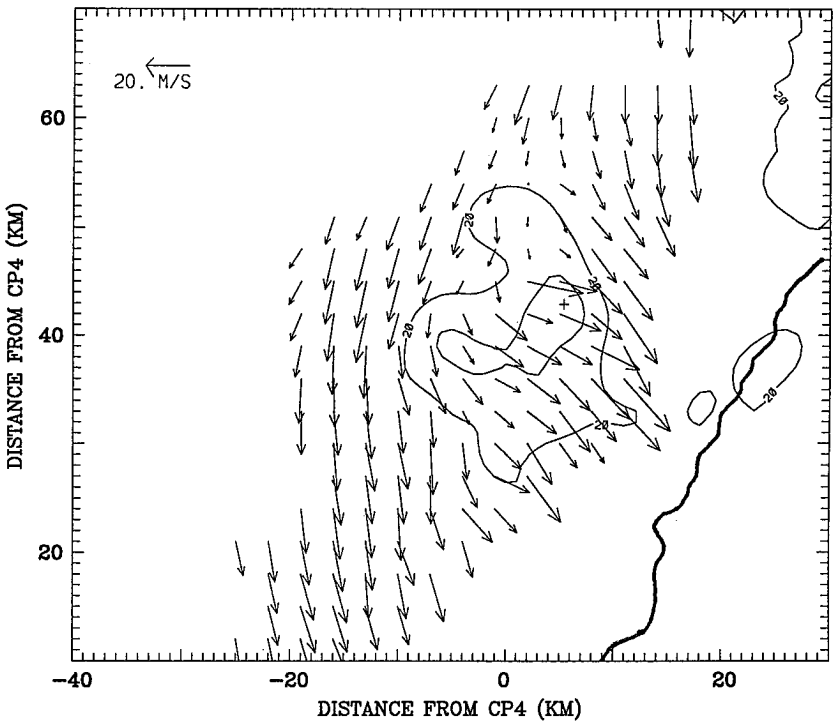

FIG. 18. Reflectivity (10-dB*Z* intervals starting from 20 dB*Z*) and horizontal winds (relative to the ground) at the 10.5-km level for 0250 LST. The scale for winds is given in the upper left side of the figure. Distances are in kilometers from the CP4 radar. The northwestern coastline is also given.

evident over the reflectivity maximum region associated with the outflow from the deep convective clouds.

b. Vertical cross sections

A series of vertical cross sections perpendicular to the rainband for 0252 LST are presented in this section to show the vertical structure across the long-lived (>2 h) reflectivity maxima at different stages of their life cycle. For these cross sections, the vectors are relative winds determined by subtracting the mean speed of the rainband from the observed winds.

Figure 19 shows the vertical structure across reflectivity maximum B along line B1–B2 in Fig. 16a. At 0250 LST, reflectivity maximum B was at its early stage of the development. The echoes tilted southeastward (right-hand side of the figure) with height, and the echo tops (10 dB*Z*) were about 8 km above the ground. Below 3 km, the barrier jet entered the rainband from the front (southeast). The maximum echo was located over the low-level convergence zone (Fig. 16b). No downward motion was observed associated with this early-stage reflectivity maximum (Fig. 19). Jorgensen and LeMone (1989) studied the statistics of updrafts and downdrafts measured by the NOAA P-3 aircraft during TAMEX. They found that the vertical velocity characteristics observed during TAMEX are similar to those observed in the Tropics (i.e., LeMone and Zipser 1980; Lucas et al. 1994a,b) but considerably lower than those over land in midlatitudes (Houze et al. 1989). Even though no aircraft measurements were made during IOP 13, it is very likely that, similar to other TAMEX clouds, convective-scale downdrafts existed within these reflectivity maxima but were not resolved by our dual-Doppler analysis.

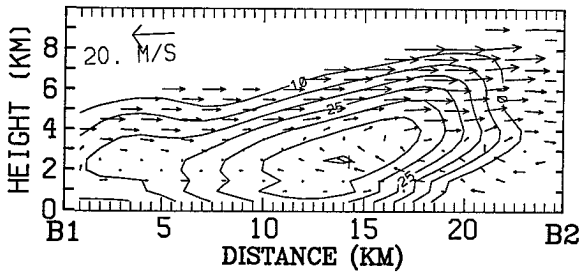

FIG. 19. Vertical cross section of the system-relative winds and reflectivity (5-dB*Z* intervals starting from 10 dB*Z*) along line B1–B2 in Fig. 16a.

At 0250 LST, reflectivity maximum A was well developed. The cross sections of the reflectivity, vertical velocity, and divergence fields through it (along line A1–A2 in Fig. 16a) are presented in Fig. 20. A reflectivity maximum (~43 dB*Z*) was located about 4 km above the surface with the echo tops (10 dB*Z*) near 15

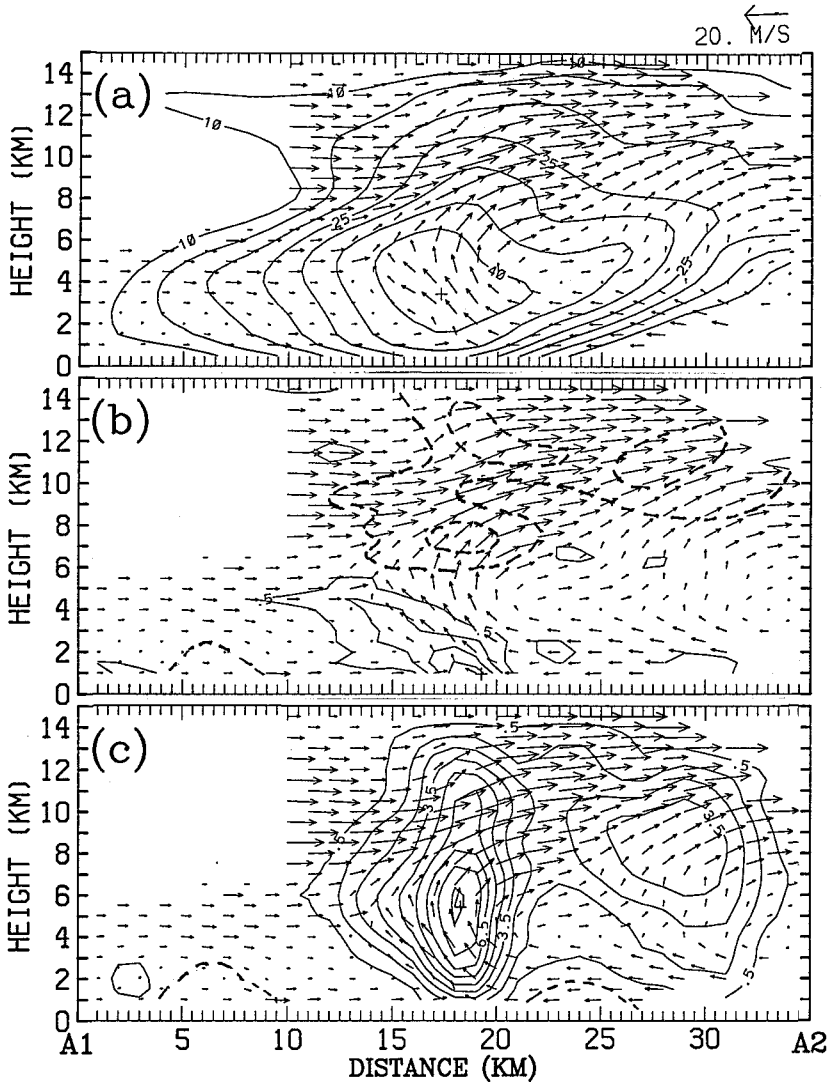

FIG. 20. Vertical cross sections of (a) reflectivity (5-dBZ intervals starting from 10 dBZ), (b) convergence, and (c) vertical velocity along line A1–A2 in Fig. 16a. The storm-relative winds are overlaid on each figure. The scale for winds is given in the upper left side of each figure. The plotting conventions for convergence (divergence) and vertical velocity fields are the same as in Figs. 16b and 16c, respectively.

km (Fig. 20a). The high reflectivities within the rainband leaned vertically southeastward (forward) in the middle and upper levels, indicating that the hydrometeors were advected southeastward by the northwesterly flow aloft. In low levels, the barrier jet entered reflectivity maximum A from the front and met the low-level westerly flow with strong convergence ($\geq 1.5 \times 10^{-3}$ s^{-1}) in the lowest 3 km (Fig. 20b). The strongest ascending motion occurred over the deep low-level convergence zone with a maximum magnitude of 8.7 m s^{-1} at about 6 km above the surface (Fig. 20c). The strong upward motion was collocated with the reflectivity core ($\geq$40 dBZ). The ascending motion tilted northwestward (backward) in low levels. A secondary inflow occurred at the 3–5 km level from the rear. The westerly flow from the rear converged with the ascending air entering from the front. The convergence zone extended upward and tilted northwestward with height. Above 5 km, the ascending motion tilted forward because of the northwesterly flow in the middle and upper troposphere. There was weak sinking motion in the lowest levels southeast of the echo maximum (Fig. 20c).

Figure 21 shows the vertical structure through a late-stage reflectivity maximum on the northeastern part of the rainband (along line I1–I2 on Fig. 16a). Compared with the other parts of the rainband, the distribution of the reflectivity was relatively homogeneous over the northeastern part of the rainband (Fig. 21a). There was

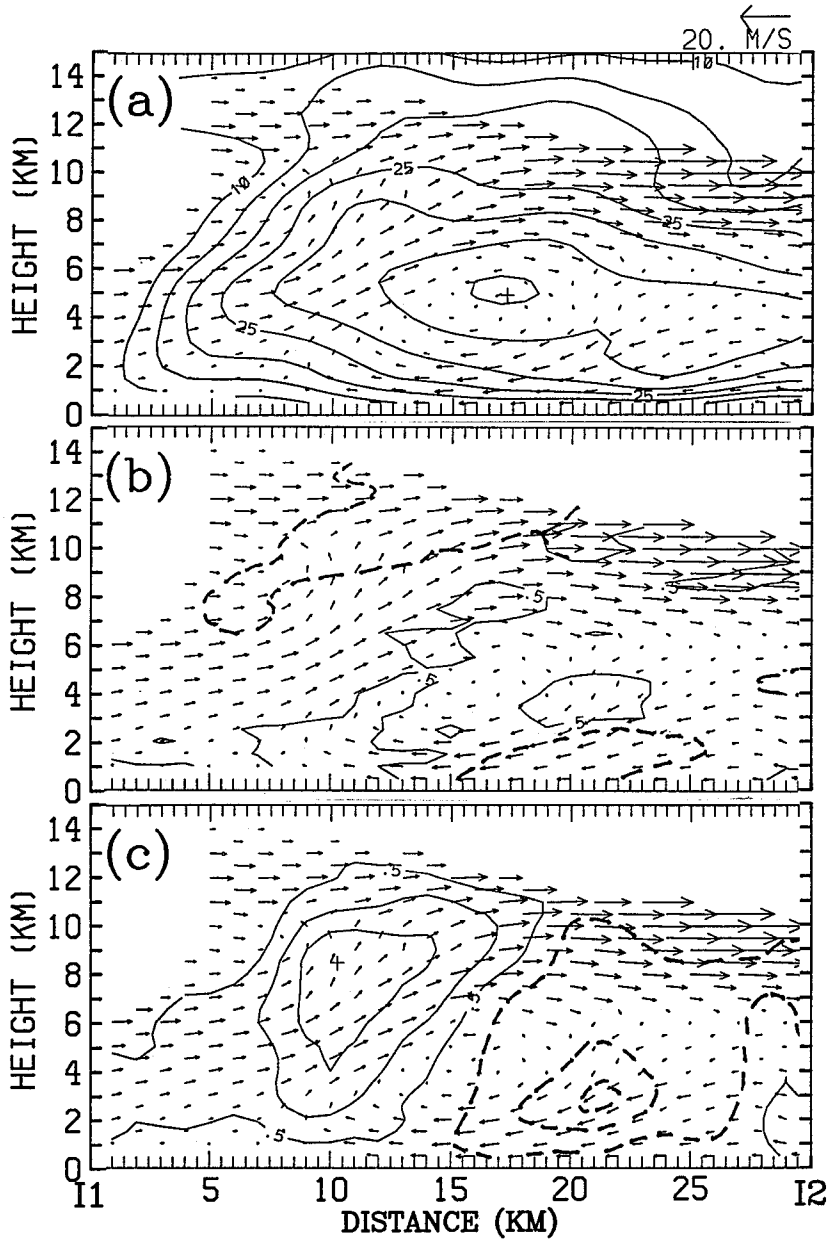

FIG. 21. Same as in Fig. 20 except for the cross sections along line I1–I2 in Fig. 16a.

a small area with reflectivity greater than 40 dBZ around 6.0 km above the ground. The maximum reflectivity was located on the southeastern side of the convergence zone (Fig. 21b). In addition to inflow from the front in the lowest 2 km, the westerly flow also entered the storm from the rear. The inflow from the rear was significant in the lowest 4–5 km. Upward motion was observed over the region where the southwesterly flow converged with the westerly flow behind the wind-shift line in low levels (Fig. 21c). The downward motion with a maximum descending velocity of 3.3 m s^{-1} at 3 km occurred just ahead of the reflectivity maximum region. The mesoscale airflow associated with the late-stage reflectivity maximum on the northeastern part of the rainband was similar to that presented by Lin et al. (1992) for reflectivity maximum E at 0653 LST (their Fig. 17).

c. A schematic diagram for mesoscale airflow associated with the rainband

Previous studies (i.e., Jou and Deng 1992; Lin et al. 1992) have focused their analyses on the late-stage reflectivity maxima on the northeastern part of the rainband. Our analysis shows that the rainband occurred in

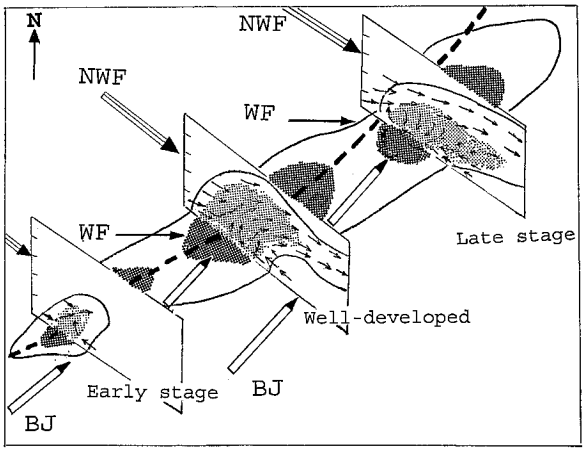

FIG. 22. Schematic diagram for the structure of the rainband. The barrier jet (BJ) converges with the westerly flow (WF) along the wind-shift line (heavy, dashed line) in low levels. The northwesterly flow (NWF) dominates in the upper troposphere. The vertical cross sections show the long-lived reflectivity maxima embedded in the rainband at the early, well developed, and late stage, respectively. The solid lines represent radar echo boundary with reflectivity core areas shaded. The thin arrows on the cross sections indicate the relative airflow to the rainband system.

a unique mesoscale environment favorable for the development and maintenance of deep convection. The most intense convection associated with the rainband occurred over a deep (~3 km), localized low-level convergence zone where the barrier jet along the coast interacted with the westerly flow behind the pressure trough in the prefrontal atmosphere.

Figure 22 shows a schematic diagram for the mesoscale airflow in the storm environment and the evolution of the long-lived reflectivity maxima embedded in the rainband. These reflectivity maxima formed on the southwestern tip of the rainband and along the low-level wind-shift line associated with the pressure trough. At the early stage of the reflectivity maxima, upward motion was observed along the wind-shift line. During their movement from the southwest to the northeast along the rainband, these maxima intensified within the low-level convergence zone where the barrier jet interacted with the westerly flow behind the wind-shift line. At the well-developed stage, radar echoes associated with the reflectivity maxima extended to high levels and leaned vertically forward (southeastward) in the middle and upper levels because the hydrometeors were advected southeastward by the northwesterly flow aloft. In addition to the low-level inflow from the front (southeast), the westerly flow also entered the storm from the rear and converged with the ascending air entering from the front. The strongest ascending motion (~9 m s^{-1}) occurred over the low-level convergence zone and was collocated with the reflectivity maximum. Upward motion was observed in the anvil with weak sinking motion in the lowest levels ahead (southeast) of the reflectivity maximum. When the reflectivity maxima moved toward the northeastern portion of the rainband and matured, the maximum reflectivity associated with them was observed southeast of the convergence zone. The inflow from the rear was significant in the lowest 4–5 km. Downward motion dominated within the reflectivity maxima in the lower troposphere. Rising motion was located northwest of the echo maximum and along the low-level wind-shift line. In the upper levels, the hydrometeors were advected southeastward by the upper-level winds. The reflectivity maxima dissipated on the northeastern end of the rainband as they moved inland. The continuous generation of new reflectivity maxima along the wind-shift line maintained the long lifetime of the rainband and produced persistent heavy rainfall along the northwestern Taiwan coast as they moved toward the coast. The heaviest rainfall occurred during the 0700–0859 LST (Fig. 2c) as the wind-shift line arrived in the northwestern coast (Fig. 13d).

7. Summary and discussion

On the morning of 25 June 1987, heavy rain occurred over northwestern Taiwan with the maximum rainfall along the northwestern coast. The large-scale conditions favorable for the heavy rainfall event included 1) the upper-level divergence in the diffluent region and 2) a conditional unstable atmosphere with abundant low-level moisture. The upper-level circulation for this case had an unique feature: The rainband developed behind (to the southwest of) an upper-level trough. When the eastward moving upper-level trough deepened northeast of Taiwan, a diffluent flow occurred over the southeastern China coast and the Taiwan area between the northeasterlies on the southeastern quadrant of the semipermanent south Asian anticyclone and the northwesterlies behind the trough. The geopotential height gradients were weak in this diffluent flow region. This region was downstream of the northwesterly jet behind the trough with significant flow deceleration. Ageostrophic winds pointing southwestward across the geopotential contours were observed over the diffluent region due to the inertial-advective effect of the horizontal winds, resulting in upper-level divergence there. The upper-level divergence occurred prior to the development of deep convection and provided the upper-level support needed for the development of heavy precipitation.

Mesoscale analysis shows the existence of a barrier jet along the northwestern coast of Taiwan resulting from the interaction between the prefrontal southwesterly flow and the island obstacle. As the Mei-Yu front advanced southeastward, the postfrontal cold air in the lowest levels was retarded by the hilly terrain along the southeastern China coast. As a result, the low-level wind-shift line associated with the 850-hPa pressure trough moved over the Taiwan Strait before the arrival of the surface front. When the low-level wind-shift line approached the northwestern coast, the westerly flow behind the trough interacted with the barrier jet. A

strong, low-level convergence zone (~3 km deep) was observed along the wind-shift line between the westerly flow coming off the southeastern China coast and the barrier jet. A rainband developed over the low-level convergence zone and moved southeastward toward the northwestern Taiwan coast with the wind-shift line. The Mei-Yu front in this case was shallow (<1 km) and moved slowly along the western coast. The convection associated with the front was weaker and shallower (echo tops below 6 km) than that developed within the deep low-level convergence zone. Behind the Mei-Yu front, the convection along the wind-shift line was also weak because the wind-shift line was undercut by the postfrontal shallow, cold northeasterly flow in the lowest levels.

There were several long-lived (>2 h) reflectivity maxima embedded in the rainband. They formed on the southwestern tip of the rainband and along the low-level wind-shift line associated with the pressure trough. These reflectivity maxima often had several individual cells with much shorter lifetimes. At the early stage of the reflectivity maxima, upward motion was observed over the low-level wind-shift line. During their movement from the southwest to the northeast along the rainband, these maxima intensified within the convergence zone where the barrier jet interacted with the westerlies behind the wind-shift line. At the well-developed stage, radar echoes associated with the reflectivity maxima extended to high levels and leaned vertically forward (southeastward) in the middle and upper levels because the hydrometeors were advected southeastward by the northwesterly flow aloft. In addition to the low-level inflow from the front (southeast), the westerly flow also entered the storm from the rear and converged with the ascending air entering from the front. The low-level convergence zone extended upward and tilted northwestward with height. The strongest ascending motion (~9 m s^{-1}) occurred over the low-level convergence zone and was collocated with the reflectivity maximum. Upward motion was observed in the anvil with weak sinking motion in the lowest levels ahead (southeast) of the reflectivity maximum. When the reflectivity maxima moved toward the northeastern portion of the rainband and matured, high reflectivities associated with them were observed southeast of the convergence zone. The westerly inflow from the rear became more significant in the lowest 4–5 km. Downward motion dominated within the reflectivity maxima in the lower troposphere. Rising motion was located northwest of the echo maximum and along the low-level wind-shift line. The reflectivity maxima dissipated on the northeastern end of the rainband as they moved inland. The continuous generation of new reflectivity maxima along the wind-shift line maintained the long lifetime of the rainband and produced persistent heavy rainfall along the northwestern Taiwan coast as they moved toward the coast. The heaviest rainfall occurred when the wind-shift line arrived in the northwestern coast.

Acknowledgments. We would like to thank all participants involved in the planning and the execution of TAMEX. Thanks also go to R. Rilling (NCAR) and S. Trier (NCAR) for their assistance in accessing NCAR CP4 and TOGA radar data, T.-C. Chen Wang (National Central University, Taiwan) for providing the universal format CAA radar data, and L. J. Miller (NCAR) and B. Anderson (NCAR) for the updated CEDRIC software package. The terrain data for Taiwan is provided by S.-S. Hong (National Central University). Part of the computing resources is supported by the Scientific Computing Division of the National Center for the Atmospheric Research, which is sponsored by the National Science Foundation. We would like to thank anonymous reviewers for their comments. This work is supported by the National Science Foundation under Grant ATM-9421060.

REFERENCES

Atlas, D., R. C. Srivastava, and R. S. Sekhon, 1973: Doppler radar characteristics of precipitation at vertical incidence. *Rev. Geophys. Space Phys.* **11,** 1–35.

Browning, K. A., and R. Wexler, 1968: The determination of kinematic wind field properties using Doppler radar. *J. Appl. Meteor.,* **7,** 105–113.

——, and T. W. Harrold, 1970: Air motion and precipitation growth at a cold front. *Quart. J. Roy. Meteor. Soc.,* **96,** 369–389.

Chen, G. T.-J., 1983: Observational aspects of the Mei-Yu phenomena in subtropical China. *J. Meteor. Soc. Japan,* **61,** 306–312.

——, 1991: Observational study on mesoscale features in Taiwan Mei-Yu season (I) (in Chinese). Tech. Rep. NSC 80-0202-M002-19, 128 pp. [Available from Prof. G. Chen, Dept. of Atmospheric Sciences, National Taiwan University, Taipei, Taiwan.]

——, and C. P. Chang, 1980: The structure and vorticity budget of an early summer monsoon trough (Mei-Yu) over southeastern China and Japan. *Mon. Wea. Rev.*, **108,** 942–953.

——, and S. S. Chi, 1980: On the frequency and speed of Mei-Yu front over southern China and the adjacent areas. *Pap. Meteor. Res.,* **3,** 31–42.

——, and J. S. Yang, 1988: On the spatial and temporal pattern of heavy rainfall in Taiwan during Mei-Yu season (in Chinese with English abstract). *Atmos. Sci.,* **16,** 151–162.

——, and C. -C. Yu, 1988: Study of low-level jet and extremely heavy rainfall over northern Taiwan in the Mei-Yu season. *Mon. Wea. Rev.,* **116,** 884–891.

Chen, S., and A. Schumann, 1990: Taiwan area mesoscale experiment: Conventional data and user's guide. NCAR Tech. Note NCAR/TN-349+1A, 123 pp. [Available from Information Services Office, NCAR, P.O. Box 3000, Boulder, CO 80307.]

Chen, Y. -L., 1993: Some synoptic-scale aspects of the surface fronts over southern China during TAMEX. *Mon. Wea. Rev.*, **121,** 50–64.

——, and N. B. -F. Hui, 1990: Analysis of a shallow front during the Taiwan area mesoscale experiment. *Mon. Wea. Rev.,* **118,** 2649–2667.

——, and ——, 1992: Analysis of a relative dry front during the Taiwan area mesoscale experiment. *Mon. Wea. Rev.,* **120,** 2442–2468.

——, and J. Li, 1995a: Large-scale conditions favorable for the development of heavy precipitation during TAMEX IOP 3. *Mon. Wea. Rev.,* **123,** 2978–3002.

——, and ——, 1995b: Characteristics of surface pressure and wind patterns over the island of Taiwan during TAMEX. *Mon. Wea. Rev.* **123,** 691–716.

——, Y. -X. Zhang, and N. B.-F. Hui, 1989: Analysis of a surface

front during the early summer rainy season over Taiwan. *Mon. Wea. Rev.*, **117,** 909–931.

——, X. A. Chen, and Y.-X. Zhang, 1994: A diagnostic study of the low-level jet (LLJ) during TAMEX IOP 5. *Mon. Wea. Rev.*, **122,** 2257–2284.

Chou, L. C., C. P. Chang, and R. T. Williams, 1990: A numerical simulation of the Mei-Yu front and the associated low-level jet. *Mon. Wea. Rev.*, **118,** 1408–1428.

Cressman, G., 1959: An operational objective analysis system. *Mon. Wea. Rev.*, **87,** 367–374.

Cunning, J. B., 1988: Taiwan area mesoscale experiment: Daily operations summary. NCAR Tech. Note NCAR/TN-305+STR, 361 pp. [Available from Information Services Office, NCAR, P.O. Box 3000, Boulder, CO 80307.]

Doviak, R. J., P. S. Ray, R. G. Strauch, and L. J. Miller, 1976: Error estimation in wind fields derived from dual-Doppler radar measurements. *J. Appl. Meteor.*, **15,** 868–878.

Houze, R. A., Jr., S. A. Rutledge, M. I. Biggerstaff, and B. F. Smull, 1989: Interpretation of Doppler weather-radar displays in midlatitude mesoscale convective systems. *Bull. Amer. Meteor. Soc.*, **70,** 608–619.

Jorgensen, D. P., and M. A. LeMone, 1989: Vertical velocity characteristics of oceanic convection. *J. Atmos. Sci.*, **46,** 621–640.

Jou, B. J., and S. M. Deng, 1992: Structure of a low-level jet and its role in triggering and organizing moist convection over Taiwan: A TAMEX case study. *Terr. Atmos. Oceanic Sci.*, **3,** 35–58.

Koch, S. E., M. DesJardins, and P. J. Kocin, 1983: An interactive Branes objective map analysis scheme for use with satellite and conventional data. *J. Climate Appl. Meteor.*, **22,** 1487–1503.

Kuo, Y.-H. and G. T.-J. Chen, 1990: The Taiwan area mesoscale experiment: An overview. *Bull. Amer. Meteor. Soc.*, **71,** 488–503.

Lee, W.-C., R. E. Carbone, and R. M. Wakimoto, 1992: The evolution and structure of a ''bow-echo–microburst'' event. Part I: The bow echo. *Mon. Wea. Rev.*, **120,** 2188–2210.

LeMone, M. A., and E. J. Zipser, 1980: Cumulonimbus vertical velocity events in GATE. Part I: Diameter, intensity, and mass flux. *J. Atmos. Sci.*, **37,** 2444–2457.

Lin, P.-L., T.-C. C. Wang, and C.-C. Yeh, 1989: Doppler observation study of a long-lived rainband in TAMEX IOP-13. *Pap. Meteor. Res.*, **12,** 91–119.

Lin, Y. -J., R. W. Pasken, and H. W. Chang, 1992: The structure of a subtropical prefrontal convection rainband. Part I: Mesoscale kinematic structure determined from dual-Doppler measurements. *Mon. Wea. Rev.*, **120,** 1816–1836.

Lucas, C., E. J. Zipser, and M. A. LeMone, 1994a: Vertical velocity in oceanic convection off tropical Australia. *J. Atmos. Sci.*, **51,** 3183–3193.

——, ——, and ——, 1994b: Convective available potential energy in the environment of oceanic and continental clouds: Correction and comments. *J. Atmos. Sci.*, **51,** 3829–3830.

Mohr, C. G., L. J. Miller, and H. W. Frank, 1986: The merger of mesoscale datasets into a common Cartesian format for efficient and systematic analysis. *J. Atmos. Oceanic Technol.*, **3,** 144–161.

Oye, R., and R. E. Carbone, 1981: Interactive Doppler editing software. Preprints, *20th Conf. on Radar Meteorology*, Boston, MA, Amer. Meteor. Soc., 683–689.

Parsons, D. B., and S. B. Trier, 1990: Taiwan area mesoscale experiment: Doppler radar operations summary. NCAR Tech. Note NCAR/TN-315+STR, 59 pp. [Available from Information Services Office, NCAR, P.O. Box 3000, Boulder, CO 80307.]

Shapiro, M. A., and P. J. Kennedy, 1981: Research aircraft measurements of jet stream geostrophic and ageostrophic winds. *J. Atmos. Sci.*, **38,** 2642–2652.

Trier, S. B., 1990: Taiwan Area Mesoscale Experiment: A guide to precipitation patterns during the 1987 field phase. NCAR Tech. Note NCAR/TN-350+STR, 333 pp. [Available from Information Services Office, NCAR, P.O. Box 3000, Boulder, CO 80307.]

——, D. B. Parsons, and T. J. Matejka, 1990: Observations of a subtropical cold front in a region of complex terrain. *Mon. Wea. Rev.*, **118,** 2449–2470.

Uccellini, L. W., and D. R. Johnson, 1979: The coupling of upper and lower tropospheric jet streaks and implications for the development of severe convective storms. *Mon. Wea. Rev*, **107,** 682–703.

Wang, S. -T., 1986: Observational analysis of the interaction between fronts and the orography in Taiwan during the late winter monsoon season. *Int. Conf. on Monsoon and Mesoscale Meteorology*, Taipei, Taiwan, National Science Council, 123–135.

Wang, T. -C. C., Y.-J. Lin, R. W. Pasken, and H. Shen, 1990: Characteristics of a subtropical squall line determined from TAMEX dual-Doppler radar data. Part I: Kinematic structure. *J. Atmos. Sci.*, **47,** 2357–2381.

Wilson, J. W., R. D. Roberts, C. Kessinger, and J. McCarthy, 1984: Microburst wind structure and evolution of Doppler radar for airport wind shear detection. *J. Climate. Appl. Meteor.*, **23,** 898–915.